Chinese Physics Letters **40**, 126101 (2023) **Express Letter**

Chiral Dirac Fermion in a Collinear Antiferromagnet

Ao Zhang(张奥)[1†], Ke Deng(邓可)[1†], Jieming Sheng(盛洁明)[1,2†], Pengfei Liu(刘鹏飞)[1†], Shiv Kumar[3], Kenya Shimada[3], Zhicheng Jiang(江志诚)[4], Zhengtai Liu(刘正太)[4], Dawei Shen(沈大伟)[4], Jiayu Li(李嘉裕)[1], Jun Ren(任俊)[1], Le Wang(王乐)[1], Liang Zhou(周良)[1], Yoshihisa Ishikawa[5], Takashi Ohhara[6], Qiang Zhang[7], Garry McIntyre[8], Dehong Yu[8], Enke Liu(刘恩克)[9], Liusuo Wu(吴留锁)[1*], Chaoyu Chen(陈朝宇)[1*], and Qihang Liu(刘奇航)[1*]

[1]*Shenzhen Institute for Quantum Science and Technology and Department of Physics, Southern University of Science and Technology, Shenzhen 518055, China*
[2]*Academy for Advanced Interdisciplinary Studies, Southern University of Science and Technology, Shenzhen 518055, China*
[3]*Hiroshima Synchrotron Radiation Centre, Hiroshima University, Higashi-Hiroshima, Hiroshima 739-0046, Japan*
[4]*State Key Laboratory of Functional Materials for Informatics and Center for Excellence in Superconducting Electronics, Shanghai Institute of Microsystem and Information Technology, Chinese Academy of Sciences, Shanghai 200050, China*
[5]*Neutron Science and Technology Center, Comprehensive Research Organization for Science and Society, Tokai, Ibaraki 319-1106, Japan*
[6]*Neutron Science Section, J-PARC Center, Japan Atomic Energy Agency, Ibaraki 319-1195, Japan*
[7]*Neutron Science Division, Oak Ridge National Laboratory, Oak Ridge, Tennessee 37831, USA*
[8]*Australian Nuclear Science and Technology Organisation, Locked bag 2001, Kirrawee DC, New South Wales 2232, Australia*
[9]*State Key Laboratory for Magnetism, Institute of Physics, Chinese Academy of Sciences, Beijing 100190, China*

(Received 30 November 2023; accepted manuscript online 4 December 2023)

In a Dirac semimetal, the massless Dirac fermion has zero chirality, leading to surface states connected adiabatically to a topologically trivial surface state as well as vanishing anomalous Hall effect. Recently, it is predicted that in the nonrelativistic limit of certain collinear antiferromagnets, there exists a type of chiral "Dirac-like" fermion, whose dispersion manifests four-fold degenerate crossing points formed by spin-degenerate linear bands, with topologically protected Fermi arcs. Such an unconventional chiral fermion, protected by a hidden $SU(2)$ symmetry in the hierarchy of an enhanced crystallographic group, namely spin space group, is not experimentally verified yet. Here, by angle-resolved photoemission spectroscopy measurements, we reveal the surface origin of the electron pocket at the Fermi surface in collinear antiferromagnet $CoNb_3S_6$. Combining with neutron diffraction and first-principles calculations, we suggest a multidomain collinear antiferromagnetic configuration, rendering the existence of the Fermi-arc surface states induced by chiral Dirac-like fermions. Our work provides spectral evidence of the chiral Dirac-like fermion caused by particular spin symmetry in $CoNb_3S_6$, paving an avenue for exploring new emergent phenomena in antiferromagnets with unconventional quasiparticle excitations.

DOI: 10.1088/0256-307X/40/12/126101

The Dirac fields obey the famous Dirac equation $(-i\alpha^i\partial_i+m\beta)\psi(x)=i\partial_0\psi(x)$, where $\alpha^i=\tau_x\otimes\sigma_i$ and $\beta=\tau_z\otimes\sigma_0$. With the operators furnishing a four-dimensional irreducible representation of the Lorentz group, the Dirac field can be decomposed into two two-component Weyl fields with opposite chiralities in the limit of zero mass. There are several manifestations of the Dirac equation in condensed matter systems, such as the quasiparticle dispersion in graphene,[1] topological insulators,[2–4] Dirac semimetals,[5–9] Weyl semimetals,[10–12] and d-wave high-temperature superconductors.[13] In Dirac semimetals, the chirality of a massless Dirac fermion must be zero because the space-time PT-symmetry (P and T denote space inversion and time reversal, respectively) forces the two branches of each doubly degenerate band to have opposite Berry curvatures [Fig. 1(a)]. Hence, the Fermi arc surface states connecting two Dirac points in a Dirac semimetal are generally not topologically protected, unlike the Fermi arc connecting chiral Weyl fermions.[14] On the other hand, chiral fermions with charge-2 chirality have been predicted and measured in materials such as CoSi,[15–19] of which the band structure manifests four-fold degeneracy

†These authors contributed equally to this work.
*Corresponding authors. Email: wuls@sustech.edu.cn; chency@sustech.edu.cn; liuqh@sustech.edu.cn

node protected by nonsymmorphic symmetry and nondegenerate bands off the high-symmetry point [Fig. 1(a)].

Recently, it is predicted that two Weyl fields with the same chirality couldbe connected together to form a "Dirac-like" fermion,[20] which manifests four-fold degenerate nodes formed by two doubly degenerate bands while carrying Chern numbers $C = \pm 2$ [Fig. 1(a)]. Interestingly, the symmetry that connects the two Weyl fields is a counterpart of isospin $SU(2)$ symmetry that relates a proton and a neutron in high-energy physics (see Section S1 of the Supplementary Materials). In solid state physics, such continuous symmetry does not exist in the framework of conventional (magnetic) crystallographic groups. Instead, the generators of such hidden $SU(2)$ symmetry belong to spin group, which involves partially decoupled spatial and spin operations,[21–23] providing a symmetry description of magnetic materials with local moments in the non-relativistic limit. Despite several predicted material candidates, such chiral Dirac-like fermions is either not experimentally observed in quantum materials, or associated with any emergent phenomena.

In this work, we provide experimental evidence of the existence of such exotic fermions in an antiferromagnet $CoNb_3S_6$, which caught great interest due to its surprisingly large anomalous Hall effect (AHE).[24–29] By angle-resolved photoemission spectroscopy (ARPES) measurements, we reveal that the electron pockets of $CoNb_3S_6$ at the Fermi surface exhibit a two-dimensional nature. Combining with neutron diffraction and first-principles calculations, we suggest a multidomain collinear antiferromagnetic (AFM) configuration, rendering the existence of the Fermi-arc surface states induced by chiral Dirac-like fermions. In addition, we discuss the effects of the chiral Dirac-like fermions as an essential element of the unexpected large anomalous Hall effect.

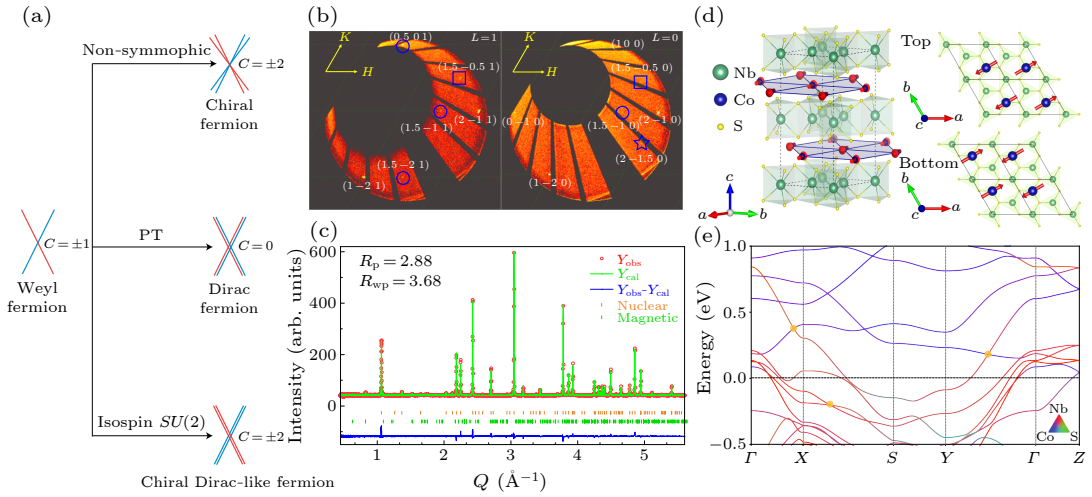

Fig. 1. Structure of the chiral Dirac-like fermion material candidate $CoNb_3S_6$. (a) Schematics of charge-1 Weyl fermion as a building block to compose charge-2 chiral fermion, Dirac fermion, and charge-2 chiral Dirac-like fermion. (b) Single-crystal neutron diffraction image in the $(H, K, L = 1)$ and $(H, K, L = 0)$ scattering plane measured at 3 K. The reflections marked by blue circles, stars and squares are from three different magnetic domains indexed by three equivalent magnetic propagation vectors, $q_{m1} = (0.5, 0, 0)$, $q_{m2} = (0, 0.5, 0)$, and $q_{m3} = (0.5, -0.5, 0)$, respectively. (c) Powder neutron diffraction pattern with Rietveld refinement fit at 10 K. (d) The AFM magnetic structure of $CoNb_3S_6$ revealed by the Rietveld refinement of powder neutron diffraction patterns. Note that due to the effect of the six magnetic M domains induced by the site point group D_3 of Co, the specific moment direction in the ab plane cannot be exactly determined. (e) Density functional theory (DFT)-calculated band structure of $CoNb_3S_6$ with the experimentally measured AFM order without spin-orbit coupling (SOC). Yellow circles indicate the positions of the chiral Dirac points.

Magnetic Structure of $CoNb_3S_6$. Our magnetization measurements suggest a phase transition around $T = 28.3$ K, with most of the moments ordered antiferromagnetically in the ab plane, and a weak ferromagnetic component along the c axis. This observation is consistent with the previous reports.[24–27] The detailed magnetization data is presented in Sections S2 and S3 of the Supplementary Materials. Figure 1(b) presents the single-crystal neutron diffraction patterns of $CoNb_3S_6$ in the $(H, K, 1)$ and $(H, K, 0)$ scattering plane at 3 K. The magnetic peaks marked by the blue circles, stars and squares can be indexed by three different magnetic wave vectors (0.5, 0, 0), (0, 0.5, 0) and (0.5, −0.5, 0), respectively, indicating three types of magnetic domains rotated 120° from each other. Due to the limited magnetic reflections of the single-crystal diffraction experiment, an additional powder neutron diffraction experiment was performed at $10\,\text{K} < T_N$ to determine the magnetic structure of $CoNb_3S_6$, as shown in Fig. 1(c). Consistent with the single-crystal diffraction results, extra weak magnetic reflections are observed and indexed by the same magnetic propagation vector $\boldsymbol{q_m} = (0.5, 0, 0)$, (0, 0.5, 0) or (0.5, −0.5, 0). Representation analysis was applied to analyze the possible magnetic structures.[30] For the space group

$P6_322$ with Co site at (1/3, 2/3, 1/4) and $\boldsymbol{q_m} = (0.5, 0, 0)$, the spin configuration can be described by four different irreducible representations. By Rietveld refinement, we found that Γ_4 could give the best fit with $R_p = 2.88$ and $R_{wp} = 3.68$ for powder neutron diffraction data. The resulting magnetic moment on the site (1/3, 2/3, 1/4) are antiferromagnetically coupled to the site (2/3, 1/3, 3/4). As schematically presented in Fig. 1(d), the refined magnetic structure of $CoNb_3S_6$ shows a collinear magnetic configuration.[31] For the intralayer, the local moments on the neighboring Co sites are antiferromagnetically coupled along the a axis, but ferromagnetically coupled along the b axis. By the refinement, we find that the Co moments are lying in the ab plane and the ordered moment of Co^{2+} is about 1.64(7) μ_B/Co. However, due to the D_3 site point group of Co^{2+} ions, the in-plane spin orientation cannot be distinguished. The detailed analysis of the magnetic structure can be found in Section S2 of the Supplementary Materials.

Emergence of Fermi-Arc Surface States. We perform DFT band structure calculation of bulk $CoNb_3S_6$ based on the measured AFM order, as shown in Fig. 1(e). Since the bands of interest are dominated by Co 3d orbitals with weak SOC, we ignore SOC for the calculations that compare with the ARPES measurement and leave the SOC effects in later discussions. There are two main features in the calculated band structure: Firstly, although PT symmetry is absent, the energy bands of any momenta are doubly degenerate. Such degeneracy is unique in magnetic materials without SOC in that it is protected by the so-called spin space group symmetry, which involves independent spin and spatial rotations compared with the conventional magnetic space group.[21,23] In $CoNb_3S_6$, the collinear AFM order guarantees $U(1)$ symmetry along the x axis $\{U_x(\theta)||E|0\}$ and a 180° pure spin rotation along the z axis followed by a fractional translation $\{U_z(\pi)||E|\boldsymbol{\tau}_{(\boldsymbol{a}+\boldsymbol{b})/2}\}$, ensuring doubly degenerate bands throughout the Brillouin zone (see Section S4.1 of the Supplementary Materials). Secondly, the band crossings are all four-fold degenerate Dirac-like points, which could appear either at arbitrary momenta or high-symmetry lines. There are multiple four-fold Dirac-like points around the calculated Fermi level and some located along Γ–X and Γ–Y lines (∼0.4 eV above the Fermi level). Interestingly, unlike the degeneracy protected by PT, all the Dirac-like points manifest Chern numbers $C = \pm 2$ rather than 0, manifesting robust Fermi-arc surface states (see Section S4.2 of the Supplementary Materials).

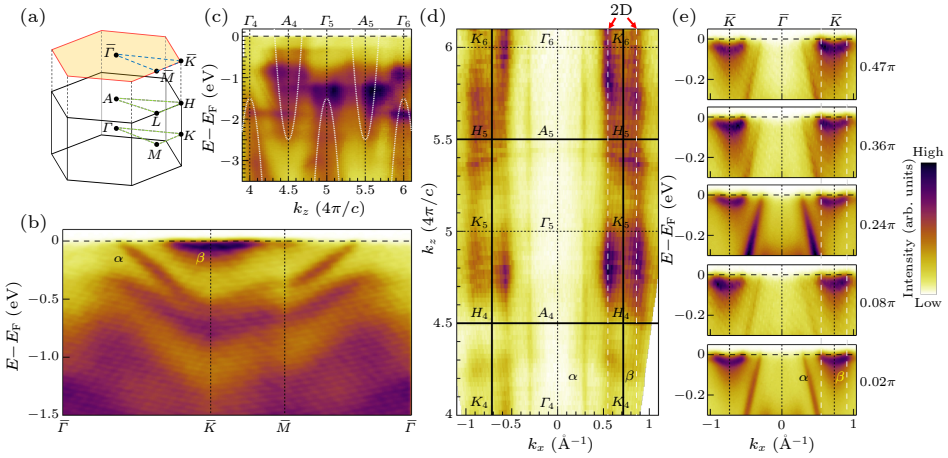

Fig. 2. Band structure and its k_z dependence of $CoNb_3S_6$ measured by ARPES at $T = 8$ K. (a) Three-dimensional bulk and 2D surface Brillouin zone of $CoNb_3S_6$. (b) Band spectrum along high-symmetry lines $\bar{\Gamma}$–$\bar{K}$–$\bar{M}$–$\bar{\Gamma}$. The hole pocket that is centered at $\bar{\Gamma}$ and crosses Fermi level is labeled as α. The electron pocket centered at $\bar{K}$ is labeled as β. (c) Spectral intensity along k_z in the direction taken with photon energies ranging from 60 to 165 eV, superposed with periodic dispersion (white dotted lines). (d) Fermi surface in k_x–k_z plane obtained by photon-energy dependent ARPES measurement. The white dashed lines in (d) indicate the k_z independence of β band. (e) Band spectra along $\bar{K}$–$\bar{\Gamma}$–$\bar{K}$ from various k_z values. White dashed lines indicate the same k_F of β at different k_z.

We next perform ARPES measurements on the natural cleavage plane (ab plane) to directly visualize the band structure of $CoNb_3S_6$. Although the AFM order enlarges the unit cell leading to a rectangular Brillouin zone (BZ), the ARPES measured spectral intensity exhibits a hexagonal symmetry matching the nonmagnetic 3D BZ [Fig. 2(a)]. This comes from the fact that ARPES spectral intensity averages photoelectrons excited from energy degenerate AFM domains with three different orientations as revealed by the neutron diffraction results. Thus, we use the nonmagnetic 3D BZ to describe the ARPES data measured at $T = 8$ K, i.e., the AFM phase. The general band structure along the high-symmetry line $\bar{\Gamma}$–$\bar{K}$–$\bar{M}$–$\bar{\Gamma}$ is shown in Fig. 2(b). Close to the Fermi level, the ARPES spectra is dominated by a hole-like, highly dispersed band (labeled as α) centered at $\bar{\Gamma}$ and an electron-like, shallow band (labeled as β) centered at $\bar{K}$. To define the precise position of high-symmetry points in the 3D BZ and uncover the k_z dependence of these bands, we perform photon-energy dependent measurements ($h\nu$ = 60–165 eV), with the momentum cut fixed along $\bar{K}$–$\bar{\Gamma}$–$\bar{K}$ direction [Figs. 2(d) and 2(e)]. As shown in Fig. 2(d) by

the Fermi surface mapping in k_z–k_x plane, both α and β bands show no observable dispersion with k_z, despite some intensity change, consistent with its layered lattice structure. The k_z periodicity can only be observed if we choose the energy window ~ 1 eV below the Fermi level and focus on the spectral intensity variation from $\bar{\Gamma}$. As shown in Fig. 2(c), broad but alternating electron-like and hole-like features can be distinguished as indicated by the superposed white dotted lines. It is noted that the k_z dispersion shows a $4\pi/c$ periodicity with lattice constant $c = 11.886$ Å, because each nonmagnetic unit cell contains two –NbS_2–$Co_{1/3}$ units.

The 2D nature of α and β bands are further elaborated by examining their dispersion at different k_z values. As shown in Fig. 2(e), we plot $\bar{K}$–$\bar{\Gamma}$–$\bar{K}$ cuts from five randomly selected k_z values, all of them show almost the same dispersion for both α and β bands. In particular, the Fermi momentum (k_F) of β band is indicated by the white dashed lines, and it remains constant with k_z, strongly demonstrating its 2D nature. Previously, this electron pocket was attributed to the bulk electronic structure and are dominated by Co atoms,[28,29] evidenced by the k_z dispersion observed by ARPES using soft x-ray photons.[27] Here we use ultraviolet photons with much higher energy and momentum resolution to clearly prove its k_z independence and will discuss its surface origin in the following.

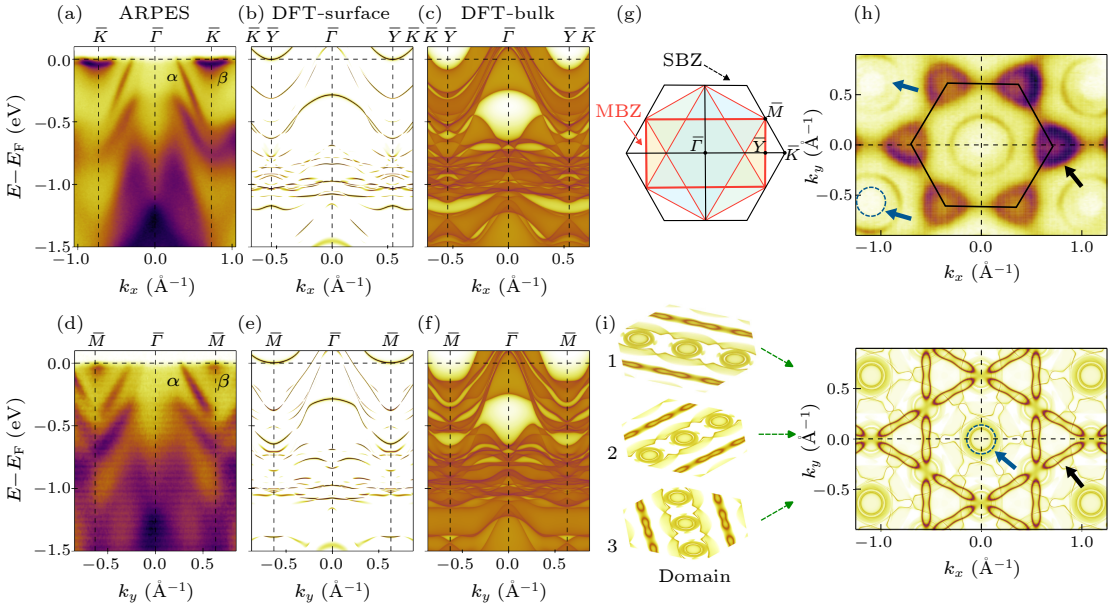

Fig. 3. Fermi-arc surface states of $CoNb_3S_6$. [(a), (d)] ARPES spectra taken with 120 eV photons along the $\bar{K}$–$\bar{\Gamma}$–$\bar{K}$ and $\bar{M}$–$\bar{\Gamma}$–$\bar{M}$, respectively. [(b), (c), (e), (f)] Projection of DFT calculated bulk and surface bands along $\bar{K}$–$\bar{Y}$–$\bar{\Gamma}$–$\bar{Y}$–$\bar{K}$ and $\bar{M}$–$\bar{\Gamma}$–$\bar{M}$, respectively. (g) Geometric relation between nonmagnetic surface BZ (SBZ, black solid lines) and antiferromagnetic BZ (MBZ, colored solid lines). (h) ARPES Fermi surface mapping with SBZ plotted. (i) Left: DFT calculated Fermi surfaces with only surface state spectral weight for the three equivalent domains. Right: superposition of the three differently orientated Fermi surfaces to construct the experimental Fermi surface with sixfold rotation symmetry.

We then compare the ARPES spectra to the projection of DFT calculated bulk and surface bands to fully demonstrate the surface origin of β band and its association with the predicted chiral Dirac-like fermions. Since the structure of $CoNb_3S_6$ is indeed stacking NbS_2 layers with a Co-layer intercalation, the calculated surface states of NbS_2 termination are adopted for comparison. We find that almost all the ARPES measured low-energy band features [including α and β bands, Figs. 3(a) and 3(d)] can be reproduced by DFT projected surface [Figs. 3(b) and 3(e)] and bulk calculations [Figs. 3(c) and 3(f)]. Figure 3(a) shows the ARPES spectra along $\bar{K}$–$\bar{\Gamma}$–$\bar{K}$. The β band centered at $\bar{K}$ comes from an electron pocket with its band bottom slightly below the Fermi level. Such a feature can be well reproduced by the DFT-calculated surface states as shown in Fig. 3(b). The ARPES spectra along $\bar{M}$–$\bar{\Gamma}$–$\bar{M}$ also reveals weak spectral weight centered at $\bar{M}$ [Fig. 3(d)]. We attribute this feature to the tail of the β surface band which locates slightly above the Fermi level at $\bar{M}$ as shown in Fig. 3(e). Such a tail is also visible for the β band at $\bar{K}$, likely from the incoherent electron scattering off other entities such as disorders, bosons, and so on.[32] In Section S4.2 of the Supplementary Materials, orbital projection analysis shows that β band is dominated by intercalated Co-3d atoms. Further calculations show that the β pocket are indeed the Fermi-arc surface states originated from the predicted chiral Dirac-like points located 0.17 eV above the Fermi level, rather than a trivial surface resonance of the bulk band [see Fig. S9(a)]. Therefore, the agreement between our photon-energy dependent ARPES measurement and DFT calculation supports a surface origin of the electron pockets.

While along $\bar{M}$–$\bar{\Gamma}$–$\bar{M}$ the ARPES and DFT surface spectra show agreement, there is a slight mismatch of the band edge (minimum) of the β pocket at $\bar{K}$ obtained from ARPES and DFT. Such discrepancy is due to the fact that our DFT calculations are based on a single-domain collinear AFM order, with the rectangular magnetic BZ (MBZ) shown in Fig. 3(g). As a result, the band edge appears at the $\bar{Y}$ point, the boundary of the MBZ. On the other hand, the ARPES spectra inevitably averages multiple magnetic domains with the same ground-state energy, thus restoring the hexagonal symmetry for the surface BZ (SBZ) and band edges appearing at the $\bar{K}$ valley ($\bar{\Gamma K} = \frac{4}{3}\bar{\Gamma Y}$). Figure 3(h) shows the measured Fermi surface indicating an identical shape and size of BZ to that of a nonmagnetic unit cell. However, the measured Fermi surface as well as the dispersion can hardly be reproduced by the nonmagnetic calculation of $CoNb_3S_6$ (see Section S4.3 of the Supplementary Materials), while the AFM order gives rise to a rectangular MBZ with lower symmetry.

To solve the dilemma, we consider three equivalent q-vectors related by C_3 rotational symmetry, rendering three energetically degenerate magnetic domains with three rectangular MBZs rotating 120° with respect to each other. Therefore, an effective hexagonal SBZ is formed, with the size identical to the nonmagnetic one [Fig. 3(g)]. The left panel of Fig. 3(i) shows the calculated surface state Fermi surfaces for each single AFM domain and illustrates the formation of the hexagonal Fermi surface by superposing the Fermi surfaces of these three equivalent domains. Figure 3(h) and the right panel of Fig. 3(i) compare the Fermi surfaces from ARPES and DFT. ARPES mapping reveals six triangular pockets centered at $\bar{K}$ formed by the β pocket [indicated by the black arrow in Fig. 3(h)]. Instead of an open line, the closed shape of such pocket is in line with the fact that the bottom of β pocket resides below the Fermi level at $\bar{K}$ and above it at $\bar{M}$ (see Section S4.2 of the Supplementary Materials). According to our DFT calculation, each triangular pocket is formed by three peanut-like surface pockets from three equivalent AFM domains. The broadness of the measured surface bands, as evidenced by the momentum distribution curve analysis in Section S5 of the Supplementary Materials, may smear out the fine structure of the calculated surface states, resulting into broad β band features centered at $\bar{K}$. In addition, the small pocket centered at $\bar{\Gamma}$ of the second BZ [Fig. 3(h), blue arrow and blue dashed circle] is in agreement with our DFT calculation [Fig. 3(i), blue arrow], further validating the general agreement. We note that due to the dipole matrix element effect in photoemission experiments (also see Section S6 of the Supplementary Materials), such small pocket is not visible in the first BZ. The general agreement between ARPES and DFT results throughout this work validates the above arguments and the existence of Fermi arc surface states associated to the chiral Dirac-like fermions in $CoNb_3S_6$.

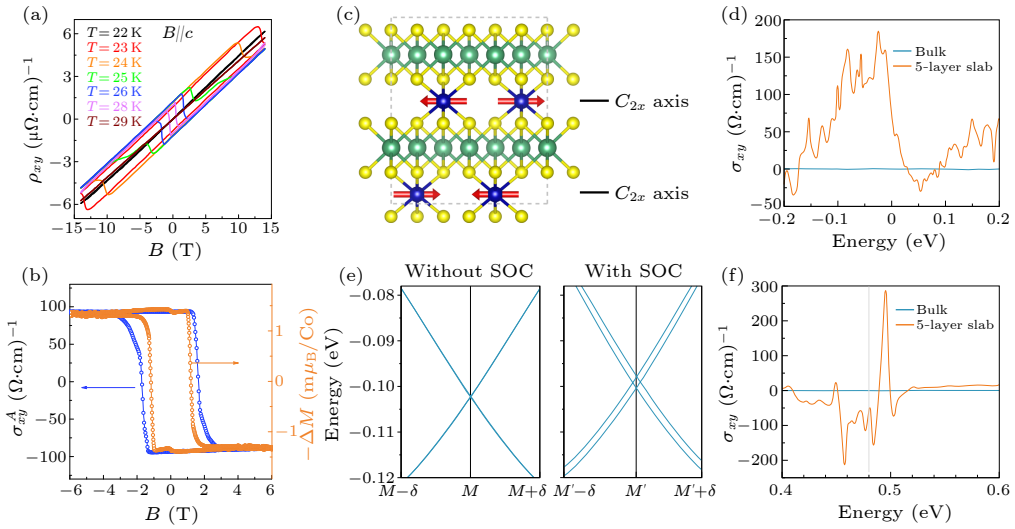

Fig. 4. Origin of the large anomalous Hall in $CoNb_3S_6$. (a) Field evolution of the Hall resistivity measured at different temperatures. (b) The anomalous Hall conductivity (blue empty circles) scales with the ferromagnetic component (orange empty circles) at $T = 26$ K. The magnetic field is along the c axis. (c) Crystal structure of $CoNb_3S_6$, where the black ticks show the plane to which rotation axis of C_{2x} exists. (d) Anomalous Hall conductivity near the Fermi level. (e) Band dispersion near a chiral Dirac point of $CoNb_3S_6$ without and with SOC, where $M = (0.4998, 0.1495, -0.0003)$, $M' = (0.4946, 0.1474, -0.0001)$, $\delta = (0.1000, 0.0000, 0.0000)$. Anomalous Hall conductivity σ_{xy} of Bulk and 5-layer slab calculated near the energy level of chiral Dirac points shown in (f), where the grey dashed line shows the energy level of chiral Dirac point (0.48 eV).

Anomalous Hall Effect. The most intriguing finding in the $CoNb_3S_6$ system is the emergence of a substantial anomalous Hall effect, accompanied by a small but not negligible net magnetic moment.[24–27,33] These results are also verified by our transport measurements. Figure 4(a) presents the field evolution of the Hall resistivity measured

from 22 K to 29 K with $I||a$ and $B||c$. For $T = 29\,\mathrm{K} > T_\mathrm{N}$, linear dependence of the Hall resistivity as a function of magnetic field [brown line in Fig. 4(a)] was observed. The positive slope of the Hall resistivity suggests that holes are the majority charge carriers in $CoNb_3S_6$. When the temperature is below 23 K, the coercive field becomes larger than 14 T. By subtracting the linear ordinary Hall background and using $\sigma^A_{xy} = \rho^A_{xy}/[(\rho^A_{xy})^2 + (\rho_{xx})^2]$, a large anomalous Hall conductivity $\sigma^A_{xy} \sim 92\,[\Omega\cdot\mathrm{cm}]^{-1}$ was obtained at 26 K [Fig. 4(b)]. More detailed information is presented in Section S7 of the Supplementary Materials. To examine the ferromagnetic contribution to the anomalous Hall conductivity, the field dependent ferromagnetic component $(-\Delta M)$ along the c axis is plotted as well [orange empty circles in Fig. 4(b)]. The measured ΔM is $\sim 0.001\,\mu_\mathrm{B}$/Co, which seems too insignificant to induce a fairly large AHE. Such a strong scaling between the AHE and ferromagnetic canting ΔM could be explained by the large hidden Berry curvature due to the chiral Dirac-like fermions.

Due to the symmetry operation of time-reversal combined with nonsymmorphic translation $\{T||E|\tau_{(\boldsymbol{a}+\boldsymbol{b})/2}\}$ (see Section S4.1 and Table S2 in the Supplementary Materials), bulk $CoNb_3S_6$ cannot exhibit finite anomalous Hall conductivity. However, rather than being intrinsically absent, the Berry curvature originated from the nontrivial bands is large yet compensated by the global high symmetry.[34,35] Therefore, the small ferromagnetic (FM) canting along the z-axis and finite SOC play a role of symmetry breaking that reveals the large Berry curvature effect hidden in the otherwise doubly degenerate bands, thus leading to finite anomalous Hall effect. Here we consider bulk and 5-layer thin film $CoNb_3S_6$ with the experimental AFM order. Our calculations show that, although bulk states exhibit anomalous Hall conductivity (AHC) smaller than $1\,[\Omega\cdot\mathrm{cm}]^{-1}$ under small magnetic canting, large AHC approaching 185 $[\Omega\cdot\mathrm{cm}]^{-1}$ emerges for the thin film when the chemical potential is 0.01–0.03 eV below the theoretical Fermi level [Fig. 4(d)]. The remarkable difference between bulk $CoNb_3S_6$ and the thin film could be attributed to the fact that all the rotation symmetries in thin-film $CoNb_3S_6$ are broken even without small magnetic canting (see Section S8.1 and Table S3), as is shown in the crystal structure of $CoNb_3S_6$ [Fig. 4(c)].

There are quite a few chiral Dirac-like fermions near the Fermi level, when considering SOC, some of them split to a twin pair of conventional Weyl points with identical chirality [Fig. 4(e)] and others are gapped. Since chiral Dirac points is obstructed by the complicated generic metallic bands around the Fermi level [Fig. 1(e)]. To reveal the relationship of the chiral Dirac-like fermions and the AHC more clearly, we show another energy window (0.4–0.6 eV) where there is only one pair of chiral Dirac-like points at 0.48 eV. With SOC and FM canting, the pair of chiral fermions is gapped, leading to sharp peaks of AHC ($\sim 200\,[\Omega\cdot\mathrm{cm}]^{-1}$) around the corresponding chemical potential [Fig. 4(f)]. Therefore, the large AHE in collinear AFM $CoNb_3S_6$ results from the Berry curvature of the chiral Dirac-like fermions as well as symmetry breaking by SOC, ferromagnetic canting. Furthermore, our results are also consistent with the fact that AHC measured in thin films is much larger than that measured in thick slabs.[25]

Discussion. Except for the mechanism discussed above, due to the complexity of magnetic configuration and surface topography in $CoNb_3S_6$, other mechanisms cannot be fully ruled out. Here we discuss our findings in connection with recent progress in this particular material system, to offer a more comprehensive description reconciling observations by different experimental techniques. Notably, motivated by the anomalous transports, a triple-$\boldsymbol{q}$ AFM order has been recently reported in CoM_3S_6 (M = Ta and Nb) by using polarized neutron scattering measurements,[36,37] suggesting a "spontaneous topological Hall effect", i.e., sizable AHE originated from the noncoplanar magnetic order rather than the net moment (see Section S8.2). However, the observed transport property of $CoNb_3S_6$ exhibits remarkable sample dependency, indicating that the existence of such a tiny net moment indeed plays a crucial role. By measuring different $Co_xNb_3S_6$ samples with slightly changed Co composition ($0.92 < x < 1$), we find the correlation between the existence of net magnetization and the existence of AHE (see Section S9). These results are also confirmed by the recent measurements with varying-composition samples.[26,27] Nevertheless, the absence of AHE without net magnetization in $CoNb_3S_6$ cannot be reconciled by the triple-$\boldsymbol{q}$ scenario. In addition, according to our DFT calculation, the Fermi surface of triple-$\boldsymbol{q}$ configuration cannot well reproduce the ARPES-measured Fermi surface (see Section S10).

From the aspect of neutron diffraction, the direct evidence to distinguish triple-$\boldsymbol{q}$ magnetization and multidomain single-$\boldsymbol{q}$ configuration is still lacking. The existing zero-field polarized neutron scattering taken by Takagi *et al.*[36] unfortunately cannot provide enough information because the two magnetic structures share similar diffraction patterns and peak intensities.[25] Similar phenomena are also observed in $Na_2Co_2TeO_6$, thereby posing challenges in distinguishing between its zigzag order and triple-$\boldsymbol{q}$ order through zero-field neutron scattering.[38,39] To overcome this, high-field neutron scattering experiments are desirable to distinguish these possibilities.[38,39] However, due to the presence of a large antiferromagnetic exchange interaction (the fitted Curie–Weiss temperature is −174 K) in the $CoNb_3S_6$ system, a very high magnetic field (~ 60 T) is required to fully polarize the magnetic moments. Overall, considering all the experimental results mentioned above, the complexity of $CoNb_3S_6$ family exhibiting interesting sample dependence may imply a composite phase diagram with distinct magnetic configurations, calling for more direct evidence for future studies.

Last but not the least, we discuss the impact of our work regarding the classification and related properties of collinear AFM materials in zero SOC limit, which have

caught remarkable attention recently. The predominant example is the emerging field of altermagnetism,[40,41] with spin splitting band structures originated from the AFM order. By definition, altermagnets are a special type of AFM where the sublattices with opposite magnetic moments are symmetry connected by operations other than inversion or translation; otherwise, there is two-fold spin degeneracy throughout the Brillouin zone. On the other hand, our work reveals that for spin-degenerate AFM, there is significant difference between the two classes, i.e., the critical symmetry connecting different sublattices is inversion, or translation.[42] The former corresponds to the conventional AFM with PT symmetry, manifesting zero topological charge for a conventional Dirac semimetal. For the latter, despite spin degeneracy, the band nodes manifest nonzero topological charges (e.g., due to $\{U_z(\pi)||E|\boldsymbol{\tau}_{(\boldsymbol{a}+\boldsymbol{b})/2}\}$ in $CoNb_3S_6$), corresponding to chiral Dirac semimetal. Therefore, our work reveals unconventional properties in a class of spin-degenerate AFM, paving an avenue for exploring unexpected emergent phenomena for AFM spintronics.

Sample Growth. Single crystals of $CoNb_3S_6$ were grown by chemical vapor transport using iodine as the transport agent. Cobalt powder (99.998%), niobium wire (99.995%) and sulfur powder (99.998%) in 1 : 3 : 6 molar ratio were loaded together with 0.3 g of iodine in a silica tube of 17 mm inner diameter and 150 mm length. After being evacuated down to 10^{-3} Pa and sealed, the tube was placed in a two-zone horizontal tube furnace, and the source and growth zones were raised to 1123 K and 1023 K, and then held for seven days. The hexagonal black crystals with lateral dimensions up to several millimeters can be obtained.

Magnetization and Electric Transport. The magnetization measurements were performed on a Quantum Design magnetic property measurement system with a single crystal mounted on a quartz stick. The electric transport measurements were performed on a 14 T Quantum Design physical property measurements system with a conventional 4-probe method. Al wires of 25 μm diameter were attached to the sample by using a wire bonding machine. An electric current of 2 mA was applied along the a axis, and the magnetic field was oriented along the c axis.

Neutron Diffraction. The single crystal neutron diffraction experiments were carried out using a single-crystal neutron Laue diffractometer, KOALA,[43] at the OPAL reactor at ANSTO and a time-of-flight single-crystal neutron Laue diffractometer, SENJU,[44] at the Materials and Life Science Experimental Facility of the Japan Proton Accelerator Research Complex. Two different single crystals (one with AHE, the other without AHE) with dimensions of about $3\times3\times0.2\,\mathrm{mm}^3$ were used for the neutron diffraction experiments and the diffraction patterns were both collected at 3 K (below T_N) and 40 K (above T_N), respectively. The powder neutron diffraction experiment was performed on the time-of-flight powder diffractometer, POWGEN,[45] at the Spallation Neutron Source at Oak Ridge National Laboratory. The powder sample with a total mass of ∼ 1 g was prepared by grinding about hundreds of single crystals and the powder neutron diffraction data were acquired between 10 K and 300 K using the 0.8 and 2.67 Å instrumental configurations. All of the neutron diffraction data were analyzed using the Rietveld refinement program FULLPROF suite.[46]

Angle-resolved Photoemission Spectroscopy Experiments. The ARPES measurement was taken with 60–165 eV photons and a Scienta Omicron DA30 analyzer. The sample was cleaved in ultra-high vacuum with pressure lower than 1×10^{-10} torr. During the measurement, the temperature of the sample was kept at around 8 K. The beam spot of the light is less than 50 μm.

First-Principles Calculations. The first-principles calculations were carried out using projector-augmented-wave method,[47] implemented in Vienna *ab initio* simulation package (VASP)[48] within the framework of density-functional theory.[49,50] The exchange and correlation effects were accounted by the generalized gradient approximation (GGA) with the Perdew–Burke–Ernzerhof formalism.[51] A cut-off energy of 520 eV is used in our calculations. The whole Brillouin-zone was sampled by $5\times8\times4$ Monkhorst–Pack grid[52] for all cells. Due to the local magnetic moments contributed from 3d electrons in Co atoms, GGA + U approach[53] within the Dudarev scheme[54] is applied and we set the U on Co to be 1 eV, which produces local magnetic moments of 1.8 μ_B consisting well with the experiments.[31] A tight-binding Hamiltonian is obtained base on maximally localized Wannier functions[55,56] of Co-3d, Nb-4d, S-3p orbitals, from which the topological surface states and Chern number are calculated. Iterative Green's function implemented in WannierTools package is used for surface states calculations.[57]

Acknowledgements. We thank Professor Jia-Xin Yin for helpful discussions. This work was supported by the National Key R&D Program of China (Grant Nos. 2020YFA0308900 and 2022YFA1403700), the National Natural Science Foundation of China (Grant Nos. 12074163, 12134020, 11974157, 12104255, 12004159, and 12374146), Guangdong Provincial Key Laboratory for Computational Science and Material Design (Grant No. 2019B030301001), the Science, Technology and Innovation Commission of Shenzhen Municipality (Grant Nos. ZDSYS20190902092905285 and KQTD20190929173815000), Guangdong Basic and Applied Basic Research Foundation (Grant Nos. 2022B1515020046, 2021B1515130007, 2022A1515011915, 2019A1515110712, and 2022B1515130005), Shenzhen Science and Technology Program (Grant Nos. RCJC20221008092722009 and RCBS20210706092218039), the Guangdong Innovative and Entrepreneurial Research Team Program (Grant No. 2019ZT08C044), Center for Computational Science and Engineering and Core Research Facilities of Southern University of Science and Technology. The authors would also like to acknowledge the beam time awarded by Australia's Nuclear Science and

Technology Organisation (ANSTO) (Grant No. P8130). The neutron experiment at the Materials and Life Science Experimental Facility of the Japan Proton Accelerator Research Complex (J-PARC) was performed under a user program (Proposal No. 2019B0140). The ARPES measurement was performed at the Hiroshima Synchrotron Radiation Center (HiSOR) of Japan (Grant Nos. 22BG023 and 22BG029), and Shanghai Synchrotron Radiation Facility (SSRF) BL03U (Grant No. 2022-SSRF-PT-020848). The authors acknowledge the assistance of SUSTech Core Research Facilities.

References

[1] Novoselov K S, Geim A K, Morozov S V, Jiang D, Katsnelson M I, Grigorieva I V, Dubonos S V, and Firsov A A 2005 *Nature* **438** 197
[2] Fu L, Kane C L, and Mele E J 2007 *Phys. Rev. Lett.* **98** 106803
[3] Moore J E and Balents L 2007 *Phys. Rev. B* **75** 121306
[4] Shen S Q 2012 *Topological Insulators*. In: *Springer Series in Solid-State Sciences* vol 174 (Berlin: Springer)
[5] Young S M, Zaheer S, Teo J C Y, Kane C L, Mele E J, and Rappe A M 2012 *Phys. Rev. Lett.* **108** 140405
[6] Wang Z J, Sun Y, Chen X Q, Franchini C, Xu G, Weng H M, Dai X, and Fang Z 2012 *Phys. Rev. B* **85** 195320
[7] Wang Z J, Weng H M, Wu Q S, Dai X, and Fang Z 2013 *Phys. Rev. B* **88** 125427
[8] Yang B J and Nagaosa N 2014 *Nat. Commun.* **5** 4898
[9] Hua G Y, Nie S M, Song Z D, Yu R, Xu G, and Yao K L 2018 *Phys. Rev. B* **98** 201116
[10] Wan X G, Turner A M, Vishwanath A, and Savrasov S Y 2011 *Phys. Rev. B* **83** 205101
[11] Fang C, Gilbert M J, Dai X, and Bernevig B A 2012 *Phys. Rev. Lett.* **108** 266802
[12] Armitage N P, Mele E J, and Vishwanath A 2018 *Rev. Mod. Phys.* **90** 015001
[13] Altland A, Simons B D, and Zirnbauer M R 2002 *Phys. Rep.* **359** 283
[14] Kargarian M, Randeria M, and Lu Y M 2016 *Proc. Natl. Acad. Sci. USA* **113** 8648
[15] Rao Z C *et al.* 2019 *Nature* **567** 496
[16] Yuan Q Q *et al.* 2019 *Sci. Adv.* **5** eaaw9485
[17] Xu X T *et al.* 2019 *Phys. Rev. B* **100** 045104
[18] Huber N *et al.* 2022 *Phys. Rev. Lett.* **129** 026401
[19] Yu Z M, Zhang Z, Liu G B, Wu W, Li X P, Zhang R W, Yang S A, and Yao Y 2022 *Sci. Bull.* **67** 375
[20] Liu P F, Zhang A, Han J Z, and Liu Q H 2022 *Innovation* **3** 100343
[21] Brinkman W F and Elliott R J 1966 *Proc. R. Soc. A* **294** 1438
[22] Litvin D B and Opechowski W 1974 *Physica* **76** 538
[23] Liu P F, Li J Y, Han J Z, Wan X G, and Liu Q H 2022 *Phys. Rev. X* **12** 021016
[24] Ghimire N J, Botana A S, Jiang J S, Zhang J J, Chen Y S, and Mitchell J F 2018 *Nat. Commun.* **9** 3280
[25] Tenasini G *et al.* 2020 *Phys. Rev. Res.* **2** 023051
[26] Mangelsen S, Zimmer P, Nather C, Mankovsky S, Polesya S, Ebert H, and Bensch W 2021 *Phys. Rev. B* **103** 184408
[27] Tanaka H *et al.* 2022 *Phys. Rev. B* **105** L121102
[28] Yang X P *et al.* 2022 *Phys. Rev. B* **105** L121107
[29] Popčević P *et al.* 2022 *Phys. Rev. B* **105** 155114
[30] Bertaut E F 1968 *Acta Cryst. A* **24** 217
[31] Parkin S S P, Marseglia E A, and Brown P J 1983 *J. Phys. C* **16** 2765
[32] Damascelli A, Hussain Z, and Shen Z X 2003 *Rev. Mod. Phys.* **75** 473
[33] Gu P *et al.* 2023 arXiv:2306.09616 [cond-mat.mes-hall]
[34] Gao A Y *et al.* 2021 *Nature* **595** 521
[35] Chen R, Sun H P, Gu M, Hua C B, Liu Q, Lu H Z, and Xie X C 2022 *Natl. Sci. Rev.* **2022** nwac140
[36] Takagi H *et al.* 2023 *Nat. Phys.* **19** 961
[37] Park P *et al.* 2023 arXiv:2303.03760 [cond-mat.str-el]
[38] Chen W J *et al.* 2021 *Phys. Rev. B* **103** L180404
[39] Yao W L, Zhao Y, Qiu Y M, Balz C, Stewart J R, Lynn J W, and Li Y 2023 *Phys. Rev. Res.* **5** L022045
[40] Šmejkal L, Sinova J, and Jungwirth T 2022 *Phys. Rev. X* **12** 031042
[41] Šmejkal L, Sinova J, and Jungwirth T 2022 *Phys. Rev. X* **12** 040501
[42] Chen X, Ren J, Li J, Liu Y, and Liu Q 2023 arXiv:2307.12366 [cond-mat.mtrl-sci]
[43] Edwards A J 2011 *Aust. J. Chem.* **64** 869
[44] Ohhara T *et al.* 2016 *J. Appl. Crystallogr.* **49** 120
[45] Huq A, Hodges J P, Gourdon O, and Heroux L 2011 *Z. Kristallogr. Proc.* **1** 127
[46] Rodríguez-Carvajal J 1993 *Physica B* **192** 55
[47] Kresse G and Joubert D 1999 *Phys. Rev. B* **59** 1758
[48] Kresse G and Furthmuller J 1996 *Phys. Rev. B* **54** 11169
[49] Hohenberg P and Kohn W 1964 *Phys. Rev. B* **136** B864
[50] Kohn W and Sham L J 1965 *Phys. Rev.* **140** A1133
[51] Perdew J P, Burke K, and Ernzerhof M 1997 *Phys. Rev. Lett.* **78** 1396
[52] Monkhorst H J and Pack J D 1976 *Phys. Rev. B* **13** 5188
[53] Liechtenstein A I, Anisimov V I, and Zaanen J 1995 *Phys. Rev. B* **52** R5467
[54] Dudarev S L, Botton G A, Savrasov S Y, Humphreys C J, and Sutton A P 1998 *Phys. Rev. B* **57** 1505
[55] Mostofi A A, Yates J R, Lee Y S, Souza I, Vanderbilt D, and Marzari N 2008 *Comput. Phys. Commun.* **178** 685
[56] Marzari N, Mostofi A A, Yates J R, Souza I, and Vanderbilt D 2012 *Rev. Mod. Phys.* **84** 1419
[57] Wu Q S, Zhang S N, Song H F, Troyer M, and Soluyanov A A 2018 *Comput. Phys. Commun.* **224** 405

Supplementary Materials for "Chiral Dirac Fermion in a Collinear Antiferromagnet"

Ao Zhang[1†], Ke Deng[1†], Jieming Sheng[1,2†], Pengfei Liu[1†], Shiv Kumar[3], Kenya Shimada[3], Zhicheng Jiang[4], Zhengtai Liu[4], Dawei Shen[4], Jiayu Li[1], Jun Ren[1], Le Wang[1], Liang Zhou[1], Yoshihisa Ishikawa[5], Takashi Ohhara[6], Qiang Zhang[7], Garry McIntyre[8], Dehong Yu[8], Enke Liu[9], Liusuo Wu[1*], Chaoyu Chen[1*] and Qihang Liu[1*]

[1]Shenzhen Institute for Quantum Science and Technology and Department of Physics, Southern University of Science and Technology, Shenzhen, 518055, China

[2]Academy for Advanced Interdisciplinary Studies, Southern University of Science and Technology, Shenzhen, 518055, China

[3]Hiroshima Synchrotron Radiation Centre, Hiroshima University, Higashi-Hiroshima, Hiroshima 739-0046, Japan.

[4]State Key Laboratory of Functional Materials for Informatics and Center for Excellence in Superconducting Electronics, Shanghai Institute of Microsystem and Information Technology, Chinese Academy of Sciences, Shanghai 200050, China.

[5]Neutron Science and Technology Center, Comprehensive Research Organization for Science and Society, Tokai, Ibaraki 319-1106, Japan

[6]Neutron Science Section, J-PARC Center, Japan Atomic Energy Agency, Ibaraki 319-1195, Japan

[7]Neutron Science Division, Oak Ridge National Laboratory, Oak Ridge, Tennessee 37831, USA

[8]Australian Nuclear Science and Technology Organisation, Locked bag 2001, Kirrawee DC, New South Wales 2232, Australia

[9]State Key Laboratory for Magnetism, Institute of Physics, Chinese Academy of Sciences, Beijing 100190, China

[†]These authors contributed equally to this work.

[*]Correspondence should be addressed to L.W. (wuls@sustech.edu.cn), C.C. (chency@sustech.edu.cn) and Q.L. (liuqh@sustech.edu.cn)

Contents

S1. Dirac-like field with chirality

First, we briefly review the Dirac field. Its field operators furnish a 4D irreducible representation of the Lorentz group. After that, we considered the symmetry condition supporting the flavor Weyl field. The Lorentz group is the group of Minkowski space-time symmetries obeying the principle of relativity. Such a group can be written as a combination of two disconnected pieces— $O(3,1) = SO(3,1) + P\,SO(3,1)$, where $SO(3,1)$ is a connected subgroup of $O(3,1)$. Any irreps of $SO(3,1)$ can be labeled by the irreps of two *su*(2) algebras, denoted as (j^+, j^-), with $j^{\pm} = 0, 1/2, 1, 3/2, ...$, because the Lie algebra of $SO(3,1)$ consists of six generators forming two individual *su*(2) algebras commuting with each other. Weyl fields—the simplest fields for spin-½ fermions—furnish the irrep $(0, 1/2)$ or $(1/2, 0)$ for right or left-handedness, satisfying two-component massless Weyl equations when *P* is broken. The reducible representation of $SO(3,1)$, i.e., $(0,1/2)\oplus(1/2,0)$, in the presence of *P*, becomes irreducible for the Lorentz group $O(3,1)$, giving rise to the Dirac fields.

The Dirac fields obey the famous Dirac equation, $(-i\alpha^i\partial_i + m\beta)\psi(x) = i\partial_0\psi(x)$, where $\alpha^i = \tau_x\otimes\sigma_i$ and $\beta = \tau_z\otimes\sigma_0$. It explains several new phases and phenomena such as antimatter, SOC, and Zeeman effect. However, seldom considered is the possibility of elementary spin-1/2 particles described by four-component fields having $(1/2,0)\oplus(1/2,0)$ (or equivalently, $(0,1/2)\oplus(0,1/2)$). To achieve such fields, *P* should be broken, reducing the corresponding symmetry group to $SO(3,1)$. Therefore, $(1/2,0)\oplus(1/2,0)$ would become a reducible representation, corresponding to a field that naturally decomposes into two Weyl fields. Second, additional internal symmetries need to be assumed to elevate the symmetry hierarchy of the system, rendering $(1/2,0)\oplus(1/2,0)$ representation irreducible. Internal symmetry operations are required to decouple the space-time operations according to the Coleman–Mandula theorem [1]. Furthermore, we selected them to form an $SU(2)$ group connecting two Weyl fields with the same chirality, analogous to the $SU(2)$ flavor symmetry in high-energy physics. Specifically, it is analogous to the isospin symmetry proposed by Heisenberg, pairing a proton and a neutron forming an $SU(2)$ doublet [2].

Such isospin symmetry can stabilize free and causal quantum fields that follow the representation $(1/2,0)\oplus(1/2,0)$ (and $(0,1/2)\oplus(0,1/2)$). The corresponding fields are called flavor Weyl fields, described by the following massless Dirac-like equation:

$$i\alpha^i\partial_i\psi(x) = \pm i\partial_0\psi(x), \tag{1}$$

where $\psi(x)$ denotes a four-component free field operator and $\alpha^i = \tau_i\otimes\sigma_0$. Furthermore, the energy spectrum of equation (1) is doubly degenerate owing to the protection of the additional $SU(2)$ group, resembling the role of *P* in the Dirac equation.

To construct such flavor Weyl field, we firstly assume that inversion symmetry is broken such that left-handed Weyl field and right-handed Weyl field could exist individually. Then, we further assume a four component Dirac field can be written as the form $\psi = \begin{pmatrix}\psi_L^1\\ \psi_L^2\end{pmatrix}$ where ψ_L^1 and ψ_L^2 are two left-handed and 2-component Weyl fields following the irreducible representation $(1/2,0)$ of the proper orthochronous Lorentz transformation. Then the representation matrices of the angular momentum operators and boost operators of proper orthochronous Lorentz transformation are $\boldsymbol{\mathcal{J}} = \frac{1}{2}\tau_0\otimes\boldsymbol{\sigma}$, $\boldsymbol{\mathcal{K}} = -\frac{i}{2}\tau_0\otimes\boldsymbol{\sigma}$, where τ_i and σ_j (i=0, *x*, *y*, *z*) are Pauli matrices.

Such field is reducible under proper orthochronous Lorentz transformation, to stabilize this field, we further assumes that there is an internal $SU(2)$ symmetry group with generators represented as $\boldsymbol{\mathcal{J}} = \frac{1}{2}\boldsymbol{\tau}\otimes\sigma_0$, which

implies that the elements of $SU(2)$ group transform on $\psi = \begin{pmatrix} \psi_L^1 \\ \psi_L^2 \end{pmatrix}$ by $exp(-i\boldsymbol{\theta} \cdot \frac{1}{2}\boldsymbol{\tau}) \begin{pmatrix} \psi_L^1 \\ \psi_L^2 \end{pmatrix}$, identical to the transformation properties of $SU(2)$ isospin symmetry on two quantum fields in standard model. Then, it is obvious that such field describe one particle formed by two Weyl fields connected by the internal $SU(2)$ symmetry group.

From quantum field theory, the field operator can be written as the following form

$$\psi_\ell(x) = \kappa\psi_\ell^+(x) + \mu\psi_\ell^{c-}(x), \tag{2}$$

$$\psi_\ell^+(x) = \sum_{s_1, s_2} \int \frac{d^3\boldsymbol{p}}{(2\pi)^{3/2}}\, u_\ell(\boldsymbol{p}, s_1, s_2)\, a(\boldsymbol{p}, s_1, s_2)\, e^{ipx}, \tag{3}$$

$$\psi_\ell^{c-}(x) = \sum_{s_1, s_2} \int \frac{d^3\boldsymbol{p}}{(2\pi)^{3/2}}\, v_\ell(\boldsymbol{p}, s_1, s_2)\, a^{c\dagger}(\boldsymbol{p}, s_1, s_2) e^{-ipx}, \tag{4}$$

where ℓ labels the 4 components of the field operator, $a(\boldsymbol{p}, s_1, s_2)$ and $a^{c\dagger}(\boldsymbol{p}, s_1, s_2)$ are the annihilation operator of a spin-1/2 particle and creation operator of the antiparticle, with eigenvalue of momentum operator to be $\boldsymbol{p}$, helicity s_1 ($s_1 = \pm 1/2$) and eigenvalue of third component of the internal $SU(2)$ symmetry $\mathcal{I}_z$ to be s_2 ($s_2 = \pm 1/2$). $u_\ell(\boldsymbol{p}, s_1, s_2)$ and $v_\ell(\boldsymbol{p}, s_1, s_2)$ are components of 4×1 column vectors, that are complex functions of $\boldsymbol{p}$, s_1 and s_2.

Then, by assuming the operation of internal $SU(2)$ symmetry group on $a(\boldsymbol{p}, s_1, s_2)$ to be $\sum_{\bar{s_2}} exp(-i\boldsymbol{\theta} \cdot \frac{1}{2}\boldsymbol{\sigma})_{s_2\,\bar{s_2}} a(\boldsymbol{p}, s_1, \bar{s_2})$ and follow the process of constructing field operator provided in Ref. [3], we can see that ψ can be constructed for describing massless spin-1/2 particles following the causal relation $\left[\psi_l(x), \psi_{\bar{\ell}}^\dagger(y)\right]_\mp = 0$ for $x - y$ space like. It could also be shown that this field obeys the following equation

$$\left(-\partial_0 + \alpha^i \partial_i\right)\psi(x) = 0, \tag{5}$$

where $\alpha^i = \sigma_0 \otimes \sigma_i$. This 4-component field have 4 independent variables, however, when we do not assume internal $SU(2)$ symmetry group, the field operator will reduce to operators with two independent variables, which is actually the Weyl field. Thus, this $SU(2)$ symmetry group helps to stabilize the flavor Weyl field.

S2. Magnetic structure analysis

Our single crystal neutron diffraction measurement at $T = 3$ K ($T < T_N$) revealed three magnetic propagation vectors (0.5, 0, 0), (0, 0.5, 0) and (0.5, -0.5, 0), which correspond to three equivalent magnetic domains allowed by the 3-fold rotational symmetry along the *c* axis in $CoNb_3S_6$ (see Fig. 1b). To analyze $CoNb_3S_6$'s possible magnetic structure, we used $\boldsymbol{q}_\mathbf{m}$ = (0.5, 0, 0) as the magnetic propagation vector and applied representation theory. Four different irreducible representations (IR) were used to describe the possible spin configurations for space group $P6_322$ (No. 182) with Co site at (1/3, 2/3, 1/4), as shown in Fig. S1 and Table S1.

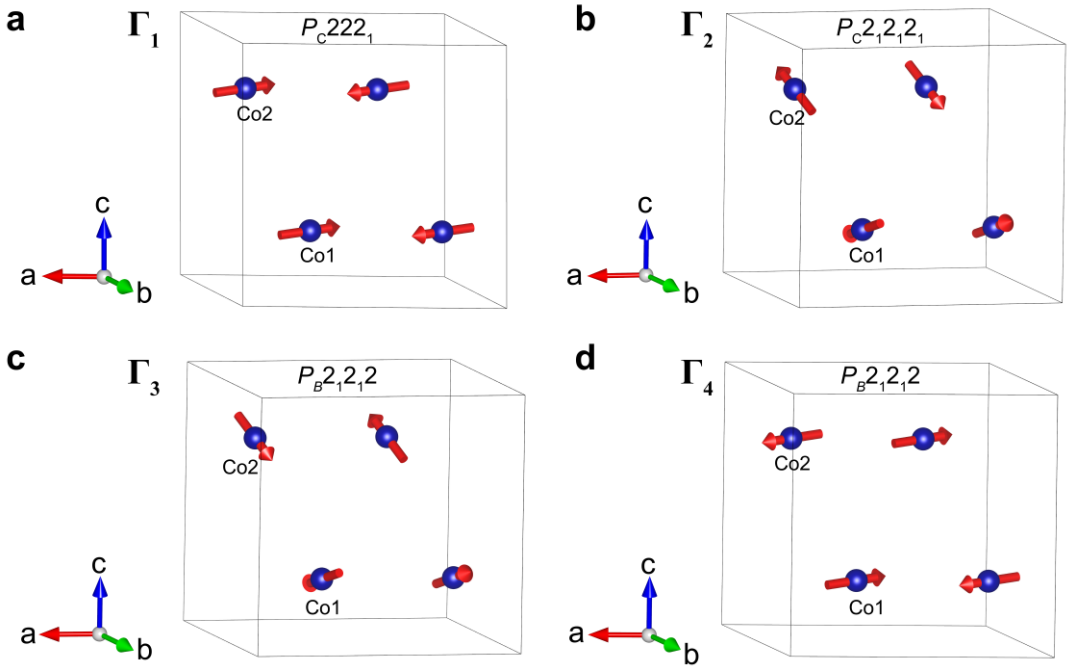

Fig. S1. The magnetic structures for the IR Γ_1, Γ_2, Γ_3 and Γ_4. For Γ_1 and Γ_4, the spins are constrained in the *ab* plane. The spin arrangement between Co_1 and Co_2 is parallel for Γ_1 and antiparallel for Γ_4. For Γ_2 and Γ_3, the spins lie in the *bc* plane. The spin components are parallel along the *b* axis and antiparallel along the *c* axis between Co_1 and Co_2 for Γ_2. In contrast, Γ_3 shows the opposite spin configuration. The magnetic space group for each IR is labeled at the top of each panel.

Table S1. Basis vectors of decomposed irreducible representations (IR) of space group $P6_322$ with magnetic wave-vector $\boldsymbol{q_m}$ = (0.5, 0, 0) and Co site at (1/3, 2/3, 1/4).

IR	Co_1 (1/3, 2/3, 1/4)	Co_2 (2/3, 1/3, 3/4)
	m_x m_y m_z	m_x m_y m_z
Γ_1	2 1 0	2 1 0
Γ_2	0 -1 0	0 -1 0
	0 0 1	0 0 -1
Γ_3	0 -1 0	0 1 0
	0 0 1	0 0 1
Γ_4	2 1 0	-2 -1 0

To distinguish these four magnetic structures for $CoNb_3S_6$, the details of magnetic neutron scattering cross section for various magnetic Bragg peaks need to be considered:

$$\sigma(q) = (\frac{\gamma r_0}{2})^2 N_m \frac{(2\pi)^3}{V_m} \langle M \rangle^2 |f(q)|^2 |F|^2 \langle 1 - (\hat{\boldsymbol{q}} \cdot \hat{\boldsymbol{s}})^2 \rangle \quad (6)$$

where $(\frac{\gamma r_0}{2})^2 = 0.07265\ barn/\mu_B^2$, N_m is the number of magnetic unit cells in the sample, V_m is the volume of the magnetic unit cell, M and $f(q)$ is the magnetic moment and magnetic form factor of Co^{2+}, respectively, F is the magnetic structure factor per magnetic unit cell, $\hat{\boldsymbol{q}}$ is the unit vector of neutron scattering vector $\boldsymbol{q}$, $\hat{\boldsymbol{s}}$ is the unit vector of the magnetic moment of Co^{2+} ions, $\langle 1 - (\hat{\boldsymbol{q}} \cdot \hat{\boldsymbol{s}})^2 \rangle$ is the polarization factor which is averaged over magnetic domains for $\boldsymbol{q_m}$ = (0.5, 0, 0).

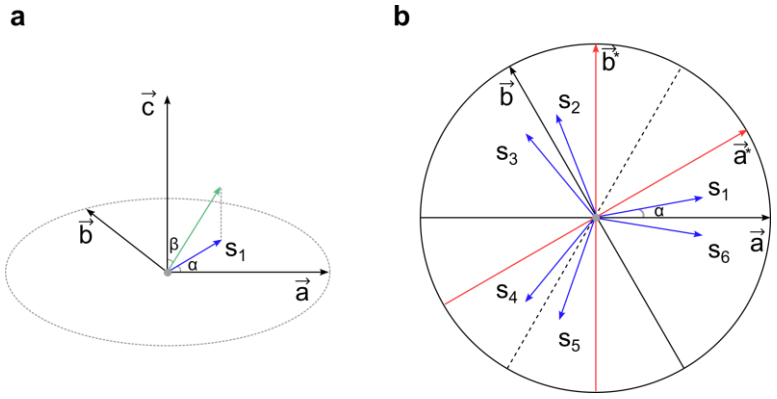

Fig. S2. **a,** An arbitrary spin (green arrow) on Co site. The angle between the spin and $\vec{c}$ axis is β, the angle between the projection of the spin (blue arrow) on the *ab* plane and $\vec{a}$ axis is α. **b,** The distribution of the six magnetic *M* domains (blue arrows) in the *ab* plane with magnetic propagation vector $\boldsymbol{q_m}$ = (0.5, 0, 0). The red arrow corresponds to the the reciprocal lattice space.

Since the Co^{2+} ions located at 2*c* Wyckoff sites with site point group D_3, for an arbitrary moment orientation, there are six magnetic *M* domains for $\boldsymbol{q_m}$ = (0.5, 0, 0), as illustrated by the blue arrows in Figs. S2a,b. The unit vector $\hat{\boldsymbol{s}}_{\boldsymbol{i}}$ of the magnetic moment for the six magnetic *M* domains can be described:

$$\hat{\boldsymbol{s}}_{\boldsymbol{1}} = \left(\frac{sin(120^\circ-\alpha)sin\beta}{sin60^\circ}, \frac{sin\alpha sin\beta}{sin60^\circ}, cos\beta\right), \tag{7}$$

$$\hat{\boldsymbol{s}}_{\boldsymbol{2}} = \left(\frac{sin\alpha sin\beta}{sin60^\circ}, \frac{sin(120^\circ-\alpha)sin\beta}{sin60^\circ}, -cos\beta\right), \tag{8}$$

$$\hat{\boldsymbol{s}}_{\boldsymbol{3}} = \left(\frac{-sin\alpha sin\beta}{sin120^\circ}, \frac{sin(60^\circ-\alpha)sin\beta}{sin120^\circ}, cos\beta\right), \tag{9}$$

$$\hat{\boldsymbol{s}}_{\boldsymbol{4}} = \left(\frac{-sin(60^\circ+\alpha)sin\beta}{sin60^\circ}, \frac{-sin(60^\circ-\alpha)sin\beta}{sin60^\circ}, -cos\beta\right), \tag{10}$$

$$\hat{\boldsymbol{s}}_{\boldsymbol{5}} = \left(\frac{-sin(60^\circ-\alpha)sin\beta}{sin60^\circ}, \frac{-sin(60^\circ+\alpha)sin\beta}{sin60^\circ}, cos\beta\right), \tag{11}$$

$$\hat{\boldsymbol{s}}_{\boldsymbol{6}} = \left(\frac{sin(60^\circ-\alpha)sin\beta}{sin120^\circ}, \frac{-sin\alpha sin\beta}{sin120^\circ}, -cos\beta\right). \tag{12}$$

Denote (*h*, *k*, *l*) as the Miller indices of the neutron scattering vector $\boldsymbol{q} = (h\boldsymbol{a}^*, k\boldsymbol{b}^*, l\boldsymbol{c}^*)$, then we have

$$\langle 1-(\hat{\boldsymbol{q}}\cdot\hat{\boldsymbol{s}})^2\rangle = 1-\frac{2(sin\beta)^2(h^2+k^2+hk)}{3a^2d^2}-\frac{(cos\beta)^2l^2}{c^2d^2}, \tag{13}$$

where $\boldsymbol{a}^* = \frac{2\pi\hat{\boldsymbol{a}}^*}{\frac{\sqrt{3}}{2}\boldsymbol{a}}$, $\boldsymbol{b}^* = \frac{2\pi\hat{\boldsymbol{b}}^*}{\frac{\sqrt{3}}{2}\boldsymbol{a}}$, $\boldsymbol{c}^* = \frac{2\pi\hat{\boldsymbol{c}}^*}{\boldsymbol{c}}$, $\boldsymbol{d} = \frac{|\boldsymbol{q}|}{2\pi} = \sqrt{\frac{4(h^2+k^2+hk)}{3a^2}+\frac{l^2}{c^2}}$. It is worth noting that the angle α disappears in the polarization factor $\langle 1-(\hat{q}\cdot\hat{s})^2\rangle$ after averaging all the six *M* magnetic domains, which means the spin direction in the *ab* plane cannot be determined by the neutron diffraction.

Due to the limited magnetic reflections of the single-crystal diffraction experiment, an additional powder neutron diffraction experiment was performed to determine the magnetic structure of $CoNb_3S_6$. Fig. S3 and Fig. S4 present the powder neutron diffraction patterns measured at 100 K and 10 K, respectively. Consistent with our single crystal

X-ray diffraction results, the Rietveld refinement of the powder neutron diffraction data at 100 K confirms the Hexagonal structure of $CoNb_3S_6$ with space group $P6_322$ (as shown in Fig. S3). For $T = 10$ K, a new set of reflections emerge around the low-Q region of the diffraction pattern, and can be indexed by the same magnetic propagation vector $\boldsymbol{q_m}$ = (0.5, 0, 0), indicating the magnetic origin. By including the six magnetic *M* domains, our Rietveld refinement shows that Γ_4 could give the best fit with $R_p = 2.88$ and $R_{wp} = 3.68$ for powder neutron diffraction data at 10 K, as shown in Fig. S4. The refined ordered moment is about 1.64(7) μ_B/Co. The schematic plot of the collinear magnetic structure is presented in Fig. 1d of the main text, yielding consistent results with the previous single crystal neutron diffraction work [4]. Note that the in-plane spin orientation cannot be distinguished due to the D_3 site point group of Co^{2+} ions. In sharp contrast, the Urbana's group [5] concluded a Γ_2 magnetic configuration with a fixed in-plane spin component along the *b*-axis (see Table S1). Therefore, the resulting magnetic structure is questionable because they ignored the effect of the six *M* magnetic domains.

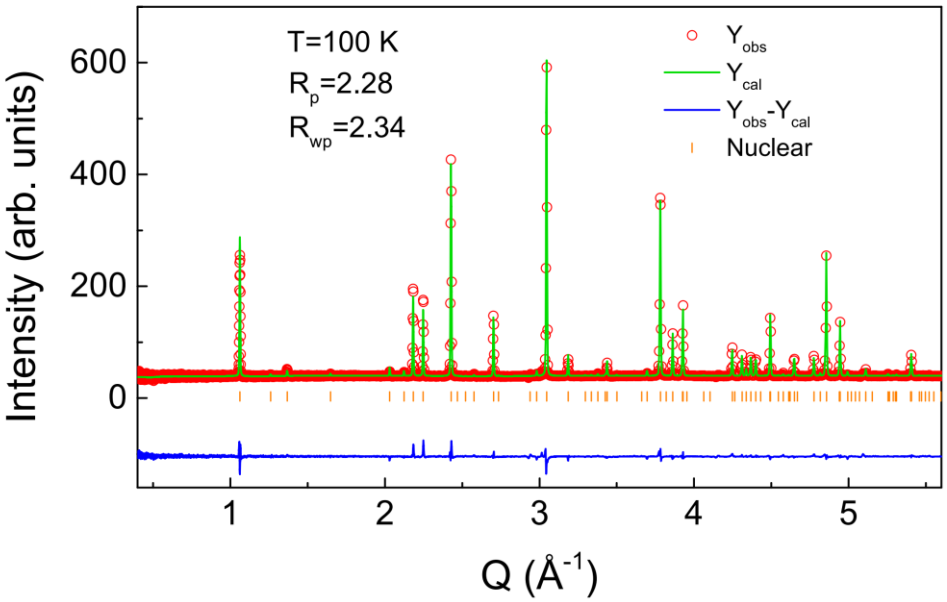

Fig. S3. Powder neutron diffraction pattern of $CoNb_3S_6$ with Rietveld refinement fit at 100 K.

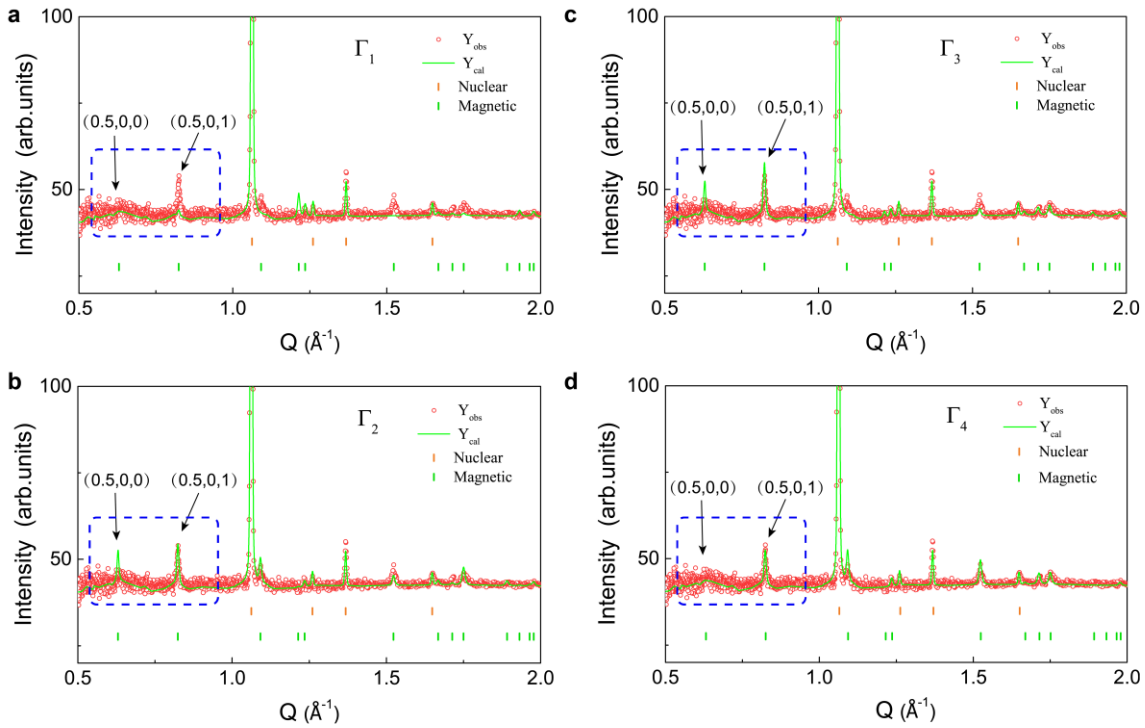

Fig. S4. The powder neutron diffraction pattern measured at 10 K with Rietveld refinement using different magnetic structure models **a,** Γ_1, **b,** Γ_2, **c,** Γ_3, **d,** Γ_4. Note that the magnetic reflections in the blue rectangle can be best fitted by Γ_4 spin configuration.

Due to the three-fold rotation symmetry C_{3z} along the z axis, besides the possibility of three equivalent magnetic domains, the compound could also form a triple-**q** magnetic order. However, diffraction from three magnetic domains with equal populations would in principle be indistinguishable from a triple-**q** magnetic order. As shown in Figs. S5a-c are the schematics of the magnetic structures for three different magnetic domains. A triple-**q** magnetic order can be understood as a vector sum of the above three magnetic domains (Figs. S5d and e).

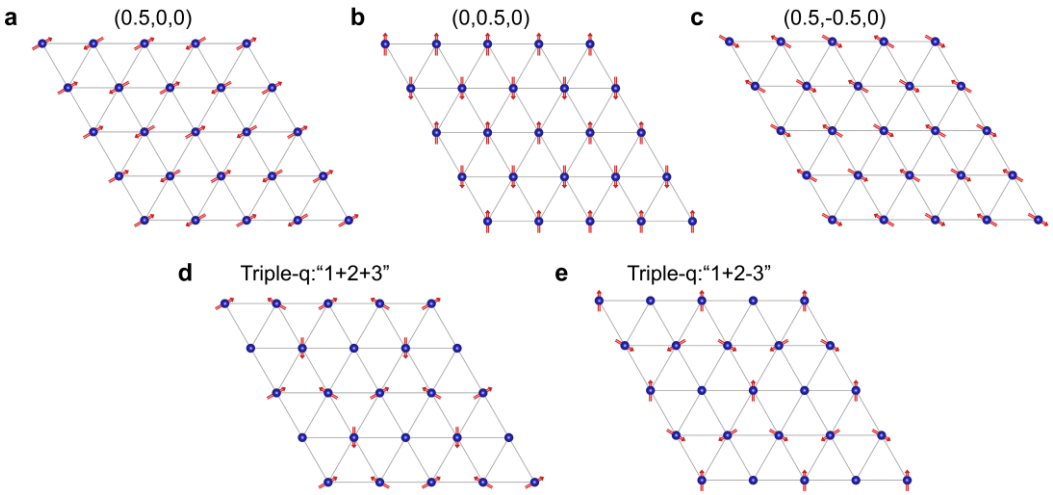

Fig. S5. The in-plane spin configurations for three equivalent magnetic propagation vectors **a,** $\boldsymbol{q}_{\mathbf{m1}}$= (0.5, 0, 0), **b,** $\boldsymbol{q}_{\mathbf{m2}}$= (0, 0.5, 0) and **c,** $\boldsymbol{q}_{\mathbf{m3}}$= (0.5, -0.5, 0). **d** and **e** are the schematics of the triple-**q** magnetic order with a vector sum of three magnetic domains "1+2+3" and "1+2-3", respectively. A total of eight domains could be expected for the triple-**q** magnetic order with different combination of the"1,2,3" three magnetic structures.

Single crystal neutron diffraction experiments were also performed on $Co_{0.92}Nb_3S_6$ (sample without AHE) at Laue diffractometers, KOALA, at the OPAL reactor at ANSTO and SENJU, at the Materials and Life Science Experimental Facility of the Japan Proton Accelerator Research Complex. Figs. S6a,b present the single-crystal diffraction image in the (H, K, L = 1) scattering plane measured at $T = 40$ K $> T_N$ and $T = 3$ K $< T_N$, respectively. For $T = 3$ K, a new set of magnetic bragg peaks emerges, which can also be indexed by the equivalent magnetic propagation vectors, $\boldsymbol{q}_{m1}$=(0.5, 0, 0) and $\boldsymbol{q}_{m3}$=(0.5, -0.5, 0), respectively. The nuclear structure refinement at $T = 3$ K further confirms $P6_322$ hexagonal structure of $Co_{0.92}Nb_3S_6$ with an R-factor $R_F = 6.94$ (Fig. S6c). Due to the weak intensity, only 5 magnetic bragg peaks indexed by $\boldsymbol{q}_m$=(0.5, 0, 0) were collected at Laue diffractometer, KOALA. By including the six magnetic *M* domains, we found the spin structure model Γ_4 can give the best fit with $R_F = 4.71$ (Fig. S6d), which indicates $Co_{0.92}Nb_3S_6$ share the same magnetic structure with $CoNb_3S_6$. The refined ordered moment for $Co_{0.92}Nb_3S_6$ is about 1.52(5) μ_B/Co, which is also comparable with the ordered moment of $CoNb_3S_6$.

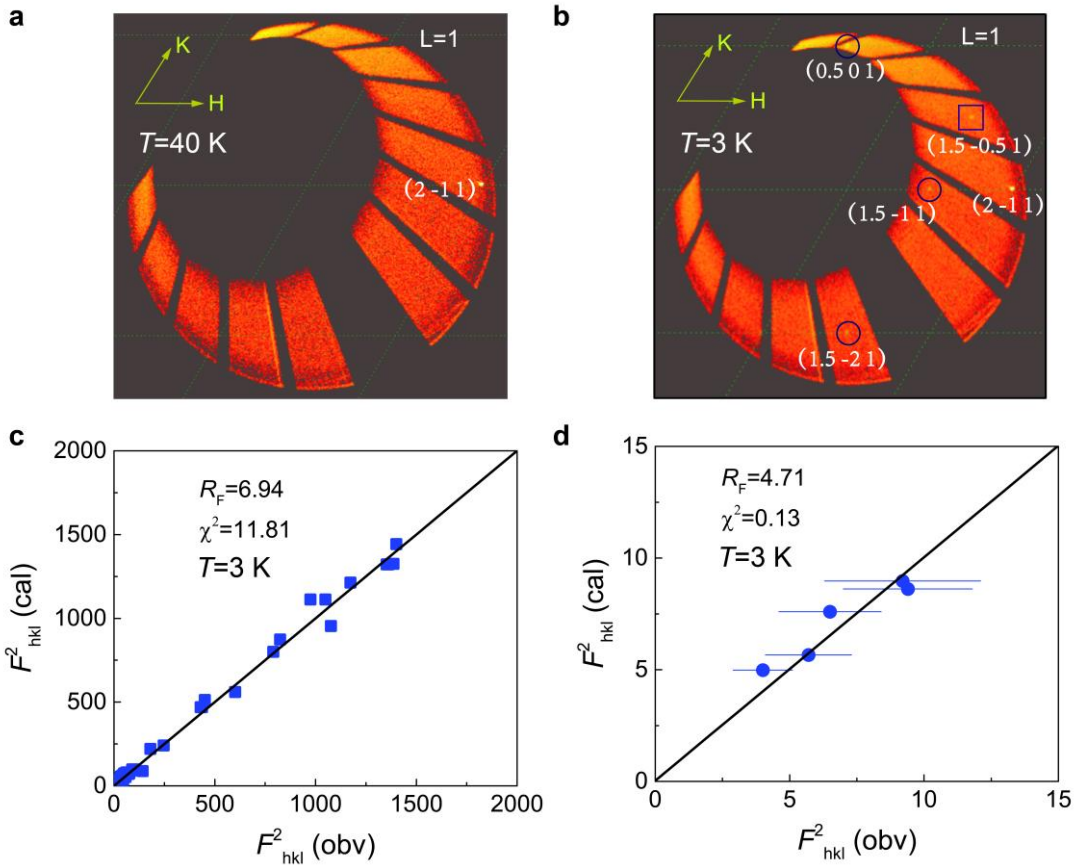

Fig. S6. Single-crystal neutron diffraction image of $Co_{0.92}Nb_3S_6$ in the (H, K, L = 1) scattering plane measured at Laue diffractometer, SENJU, with **a**, $T = 40$ K $> T_N$, **b**, $T = 3$ K $< T_N$. The reflections marked by blue circles, and squares are from two different magnetic domains indexed by equivalent magnetic propagation vectors, $\boldsymbol{q}_{m1}$ = (0.5, 0, 0) and $\boldsymbol{q}_{m3}$ = (0.5, -0.5, 0), respectively. **c**, The nuclear structure refinement of $Co_{0.92}Nb_3S_6$ at $T = 3$ K. **d**, The magnetic structure refinement of $Co_{0.92}Nb_3S_6$ at $T = 3$ K. The calculated magnetic intensities vs observation using Γ_4 spin configuration. The data used in **c** and **d** was collected at Laue diffractometer, KOALA.

S3. Magnetization measurements of $CoNb_3S_6$

Fig. S7 shows the temperature evolution of the magnetization *M(T)* measured at *H*=0.1 T with field along the *a*

and *c* axis. For *H*//*a*, the zero-field cooled (ZFC) and field cooled (FC) measurements show identical behaviors. Both the *M(T)* curves exhibit a broad peak around T = 30 K and a sharp decrease at T = 28.3 K, suggesting antiferromagnetic (AFM) phase transition in $CoNb_3S_6$. For *H*//*c*, *M(T)* curves show an irreversible behavior between the FC and ZFC measurements below T_N. The ZFC magnetization initially increases on cooling and reaches the maximum at 28.5 K, followed by an abruptly decrease around T_N = 28.3 K. Further lowering the temperature, it shows an additional upturn feature below 26.1 K. As a comparison, the FC magnetization shows an abruptly increase around T_N, reaches a maximum at 27.6 K and decreases on further cooling. These irreversible behaviors observed in *M(T)* indicate the presence of ferromagnetic component along the *c* axis.

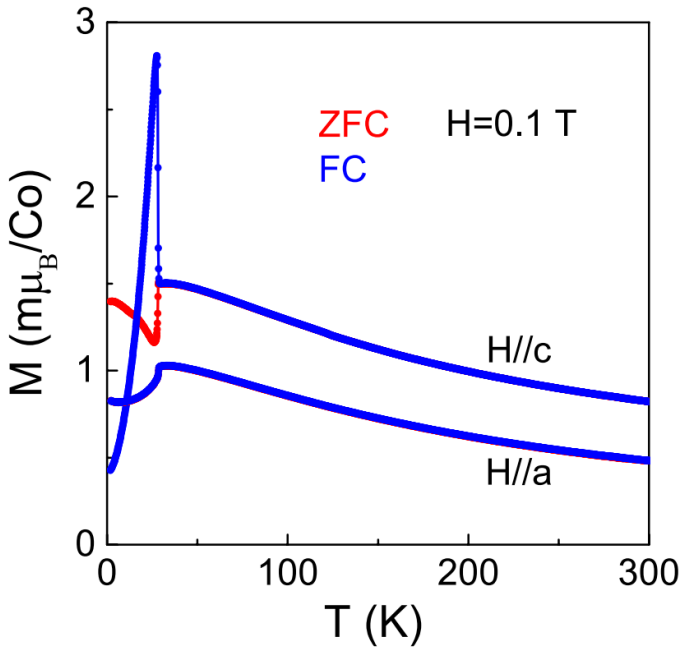

Fig. S7. Temperature dependence of the magnetization measured at *H*=0.1 T with field along the *a* and *c* axis. The blue and red lines represent the field cooled (FC) and zero field cooled (ZFC) measurements, respectively.

The isothermal magnetization *M(H)* curves, measured from 22 K to 29 K with *H*//*c*, are shown in the Fig. S8. For T = 29 K > T_N, nearly linear *M(H)* curves were observed between -7 T and 7 T, while, for $T < T_N$, a small ferromagnetic hysteresis loop gradually began to emerge, implying the ferromagnetic component was accompanied by the AFM phase transition. As lowering the temperature, the hysteresis loop gradually becomes larger due to the increase of the ferromagnetic coercive field. When the temperature is below 24 K, the coercive field becomes larger than 7 T, beyond the limit of our experimental MPMS magnet, which results in the incomplete hysteresis loops, as shown in Fig. S8b.

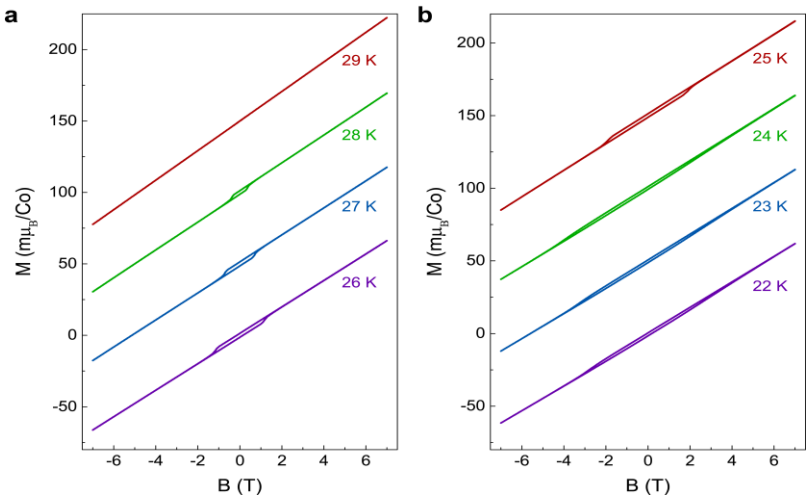

Fig. S8. Field dependence of the magnetization measured from 22 K to 29 K with field along the *c* axis.

S4. Symmetry analysis of $CoNb_3S_6$

S4.1. Doubly degenerate bands of $CoNb_3S_6$

$CoNb_3S_6$ belongs to space group $P6_322$ (No. 182). It is a collinear antiferromagnet with magnetic moments oriented along a crystal axis within the *ab* plane. This magnetic structure corresponds to the magnetic space group $P_B2_12_12$ (No. 18.22) and the spin space group $P_B{}^12_1{}^12_1{}^12\ {}^{\infty m}1$. According to previous work [6], the elements of this spin space group are listed in Table S2. From Table S2, we can prove that the element $\{U_z(\pi)||E|\boldsymbol{\tau}_{(a+b)/2}\}$ is included in the spin space group without SOC. In addition, the $\{U_z(\pi)||E|\boldsymbol{\tau}_{(a+b)/2}\}$ preserve double degeneracy in the whole Brillouin zone.

In fact,$\{U_z(\pi)||E|\boldsymbol{\tau}_{(a+b)/2}\}$is an symmetry keeping the Hamiltonian invariant, $\{U_z(\pi)||E|\boldsymbol{\tau}_{(a+b)/2}\}\varepsilon(s,\vec{k}) = \varepsilon(s,\vec{k})$. At the same time, we apply this element on the spin and momentum-dependent energy band $\varepsilon(s,\vec{k})$. Since $U_z(\pi)$ will reverse the spin, $\{U_z(\pi)||E|\boldsymbol{\tau}_{(a+b)/2}\}\varepsilon(s,\vec{k}) = \varepsilon(-s,\vec{k})$. Hence $\varepsilon(s,\vec{k}) = \varepsilon(-s,\vec{k})$. The band structure is at least double-degenerate in the whole Brillouin zone.

Table S2. Group elements of the magnetic space group and spin group describing $CoNb_3S_6$.

	Spin space group	Group elements
w/ SOC	$P_B{}^22_1{}^22_1{}^22$	H: $\{E\|\|E\|0\},\{U_x(\pi)\|\|C_x(\pi)\|0\},$ $\{U_y(\pi)\|\|C_y(\pi)\|\boldsymbol{\tau}_{(b+c)/2}\},\{U_z(\pi)\|\|C_z(\pi)\|\boldsymbol{\tau}_{(b+c)/2}\}$ M: $\{T\|\|E\|\boldsymbol{\tau}_{(a+b)/2}\},\{TU_x(\pi)\|\|C_x(\pi)\|\boldsymbol{\tau}_{(a+b)/2}\},$ $\{TU_y(\pi)\|\|C_y(\pi)\|\boldsymbol{\tau}_{(a+c)/2}\},\{TU_z(\pi)\|\|C_z(\pi)\|\boldsymbol{\tau}_{(a+c)/2}\}$
w/o SOC	Nontrivial: $P_B{}^12_1{}^12_1{}^12$	H: $\{E\|\|E\|0\},\{E\|\|C_x(\pi)\|0\},$ $\{E\|\|C_y(\pi)\|\boldsymbol{\tau}_{(a+c)/2}\},\{E\|\|C_z(\pi)\|\boldsymbol{\tau}_{(a+c)/2}\}$ M: $\{T\|\|E\|\boldsymbol{\tau}_{(a+b)/2}\},\{T\|\|C_x(\pi)\|\boldsymbol{\tau}_{(a+b)/2}\},$ $\{T\|\|C_y(\pi)\|\boldsymbol{\tau}_{(b+c)/2}\},\{T\|\|C_z(\pi)\|\boldsymbol{\tau}_{(b+c)/2}\}$
	Trivial: ${}^{\infty m}1$	$\{TU_n(\pi)\|\|E\|\|0\}\ (n = cos\varphi\hat{y} + sin\varphi\hat{z}, \varphi \in (0,\pi])$ $\{U_x(\theta)\|\|E\|\|0\}\ (\theta \in (0,2\pi])$

$\boldsymbol{\tau}_{(a+b)/2} = (1/2,1/2,0), \boldsymbol{\tau}_{(b+c)/2} = (0,1/2,1/2), \boldsymbol{\tau}_{(a+c)/2} = (1/2,0,1/2)$;

H/M: elements without/with time-reversal symmetry.

S4.2. Chern number and robust Fermi-arc surface states

From our calculated *E-k* spectra shown in Figs. S9a-b, it is clear to see that an open line connects two chiral Dirac points with opposite chiralities (i.e., N_1 and P_1). However, for the constant energy contour, such an open line can be observed when the two chiral fermions with opposite chirality have the same energy (e.g., in time-reversal preserved Weyl semimetal TaAs). Furthermore, in our ARPES measurement, the experimental Fermi level cuts the bottom of the Fermi arc surface states (see the green dashed line in Fig. S9a), leading to a small "pocket" formed by a closed line (corresponding to the peanut-like Fermi surface shown in Figure S9d). Note that while Fig. S9d considers a single magnetic cell, the Fermi surface shown in Fig. 3i takes into account three equivalent magnetic domains, thus forming the hexagonal Fermi surface pattern. Fig. S9e shows our DFT calculations that when the energy is located in between N_1 and P_1 (at 0.28 eV), the Fermi arc states exhibit open-line characteristics (black arrow). It is worth noting that we consider the (001) surface states with $\{U_z(\pi)||E|\tau_{(a+b)/2}\}$symmetry preserved, leading to twofold degenerate surface states and a Chern number of 2 (Figs. S9f,g). This is in sharp contrast to the typical topological insulators and Weyl semimetals where the surface states are nondegenerate.

In fact, Fig. S9a already clearly shows that the β pocket it is a segment of the Fermi arc surface states connecting two chiral Dirac points (see the bulk bands marked by the red box in Fig. S9a). Remarkably, the β band does not align with the adjacent bulk bands. The energy of bulk band is lower at the $\bar{M}$ point and higher at the $\bar{Y}$ point (see Figs. 3c,f). This contradicts the topological surface states observed, which is lower at the $\bar{K}$ point and higher at the $\bar{M}$ point (see Figs. 3a,d). This is also consistent with the relative energies of the surface and bulk bands for the *M* and *Y* points shown in Fig. S9a. Thus, we conclude that the β band is a result of the Fermi arc surface states, rather than surface resonances.

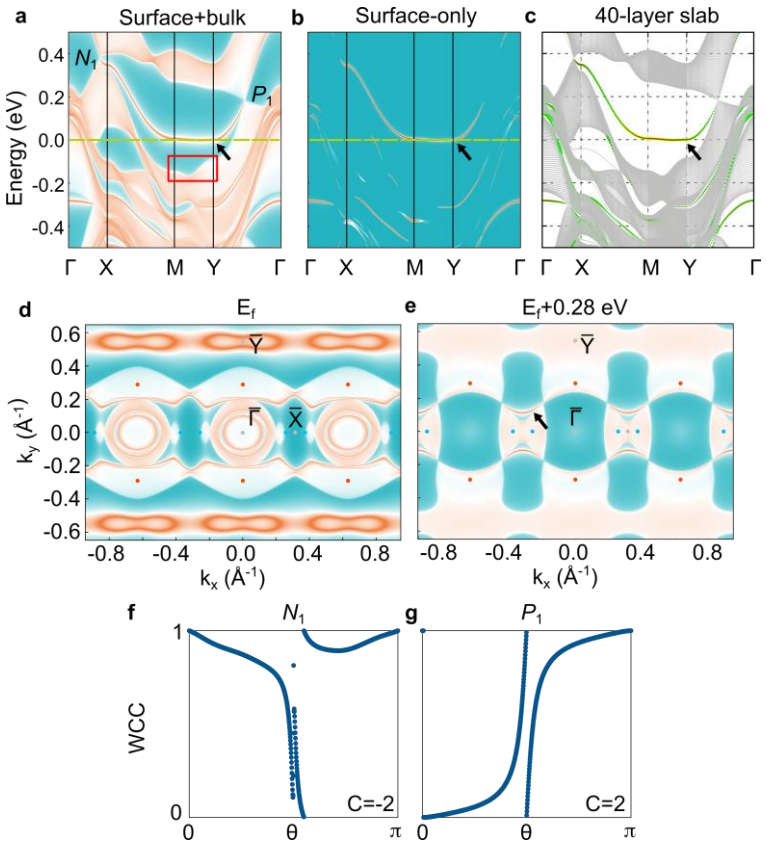

Fig. S9. The Fermi-arc surface states and Chern number of $CoNb_3S_6$. **a**, The Fermi-arc surface states of $CoNb_3S_6$ contain both bulk and surface contribution. **b**, Fermi-arc surface states of $CoNb_3S_6$ with only surface contribution. **c**,

The 40-layer slab bands calculation with projection on Co-3*d* (yellow), Nb-4*d* (green) and S-3*p* (red) orbitals in the first unit cell of NbS_2 surface. Fermi-arc surface states are denoted by black arrows. **d** and **e**, Isoenergy surface states enclosing chiral Dirac points with opposite chirality on (001) surface at Fermi energy (E_f) and 0.28 eV above Fermi energy, respectively. The green dashed line denotes the Fermi energy. The red and blue solid dots in **d** and **e** represent the positions of the chiral Dirac points with opposite chirality. **f,g** The Wannier charge centers (WCCs) of the chiral Dirac points (N_1 and P_1) and their Chern numbers. N_1 = (0.40793, 0.00008, 0.00002), P_1 = (0.00001, 0.26514, 0.00003).

S4.3. The electronic structure and fermi surface of nonmagnetic $CoNb_3S_6$

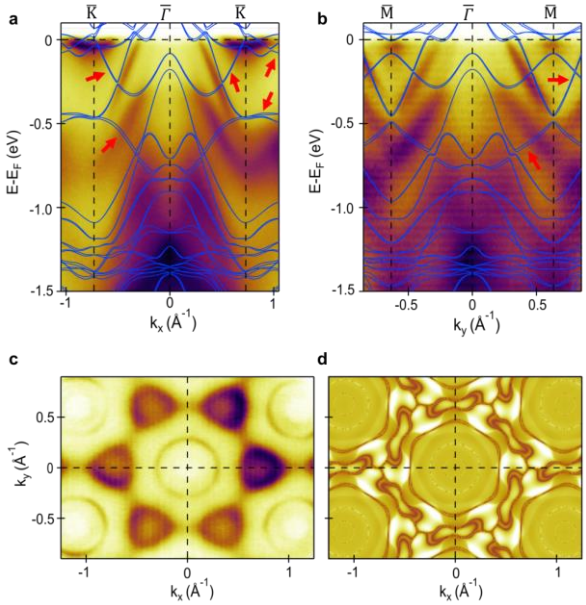

Fig. S10. The electronic structure and Fermi surface of nonmagnetic $CoNb_3S_6$. **a** and **b** ARPES spectra taken with 123 eV photons along the $\bar{K}-\bar{\Gamma}-\bar{K}$ and $\bar{M}-\bar{\Gamma}-\bar{M}$, respectively. The DFT calculation of nonmagnetic $CoNb_3S_6$ along the above two k-paths with SOC are overlaid on top of ARPES Data. The red arrows indicate the main mismatch between APRES measurement and DFT calculation. **c** and **d** denote the ARPES Fermi surface mapping and DFT calculated Fermi surface for nonmagnetic $CoNb_3S_6$, respectively.

S5. Momentum distribution curves of β at E_F

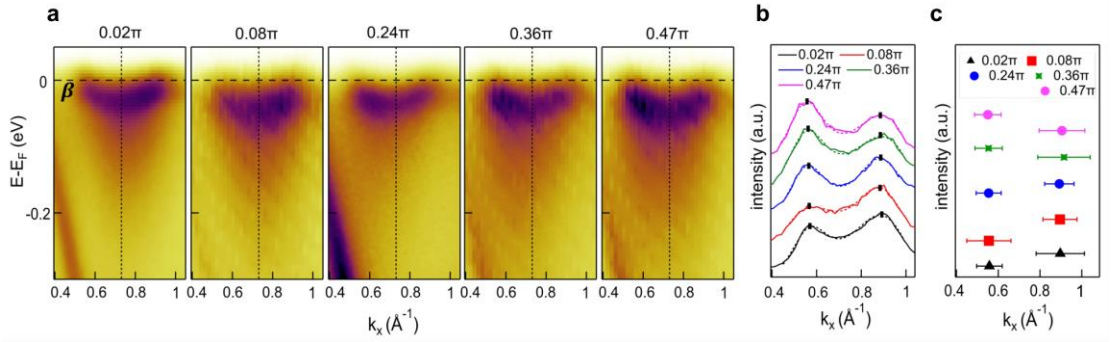

Fig. S11. The ARPES spectra and momentum distribution curves (MDCs) of β at E_F. **a,** ARPES spectra of β cuts at different k_z value along $\bar{\Gamma}-\bar{K}-\bar{\Gamma}$ direction, vertical black dashed lines denote $\bar{K}$ points. **b**, Corresponding MDCs (solid lines) for β at E_F, appended with two Lorentzian peak fitting (dashed lines). **c,** Fitted peak positions for β at E_F (k_F), with the error bars defined by FWHM of the fitted curves.

S6. ARPES spectra taken with different polarization light

Figure S12 shows ARPES spectra taken with different linear polarized photons. The β band and dispersion away from the $\bar{\Gamma}$ point are clearly resolved in the spectra taken with *p-polarized* light (Figs. S12a,c), while the dispersion at the $\bar{\Gamma}$ point are either absent or strongly suppressed. In contrast, the spectra taken with *s-polarized* light (Figs. S12b,d) clearly resolve the dispersion at the $\bar{\Gamma}$ point, but strongly suppress the dispersion away from the $\bar{\Gamma}$ point. This distinct intensity distribution of ARPES cuts with different polarized light is attributed to the dipole matrix element effect.

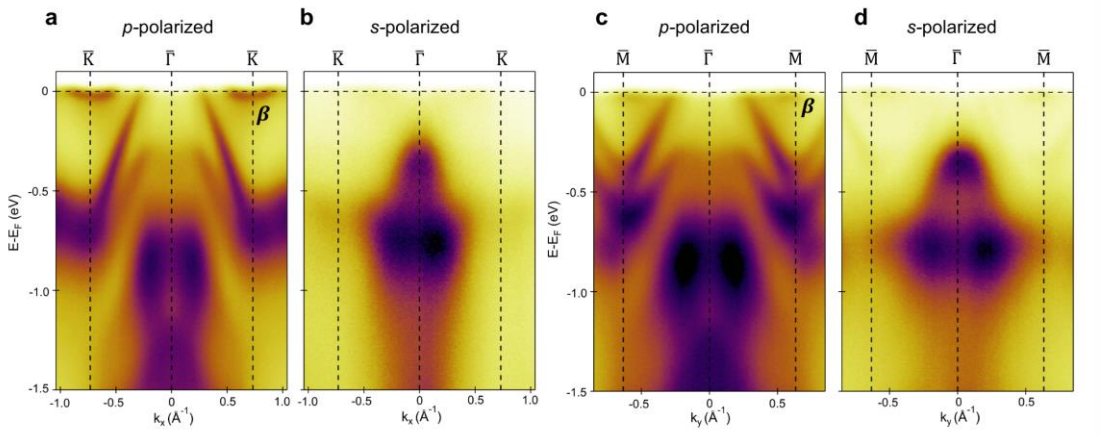

Fig. S12. ARPES spectra taken with different polarized light. **a**,**b** ARPES cuts along $\bar{K}-\bar{\Gamma}-\bar{K}$ direction taken with 80 eV LH (*p*) and LV (*s*) polarized light, respectively. **c**,**d** ARPES cuts along $\bar{M}-\bar{\Gamma}-\bar{M}$ direction taken with 80 eV *p* and *s* polarized light, respectively.

S7. Electric transport measurements

The zero-field electrical resistivity as a function of temperature measured with current along the *a* axis is presented in Fig. S13. The anomaly around 28.7 K in $\rho_{xx}(T)$ curve further confirmed the antiferromagnetic transition observed in the magnetization measurements.

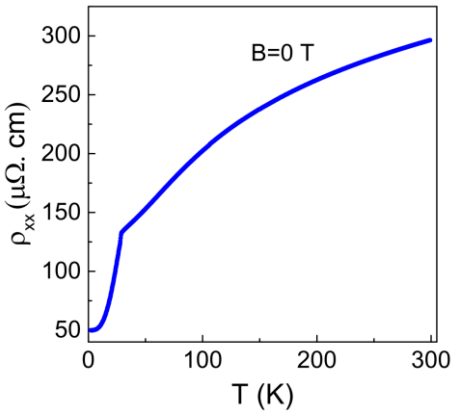

Fig. S13. Temperature dependence of the electrical resistivity with current along the *a* axis for $CoNb_3S_6$.

Fig. S14a illustrates the field dependent Hall resistivity measured between 22 K and 29 K with current along the *a* axis and field along the *c* axis. By subtracting the linear background, large anomalous Hall resistivity can be obtained for $T < T_N$, as shown in Fig. S14b. The corresponding anomalous Hall conductivity $\sigma_{xy}^{A} = \rho_{xy}^{A}/((\rho_{xy}^{A})^2 +$

$(\rho_{xx})^2$) at different temperatures are presented in Fig. S14c. As shown in Fig. S14d is the field evolution of the longitudinal resistivity ρ_{xx} measured at different temperatures. Only a small magnetoresistance (MR ~5%) is observed below T_N. The small jumps observed in the MR curves correspond to the flips of ferromagnetic components.

Fig. S15a are the ordinary Hall coefficients extracted from the linear fits of the isothermal field dependent Hall effect at different temperatures. If a single band model was assumed, the carrier concentration of the holes can be estimated by $n = 1/|eR_0|$, and presented in Fig. S15b. The temperature evolution of the carrier concentration shows a concave-like feature with the minimum around 1.4× 10^{21} cm^{-3} between 23 K and 28 K.

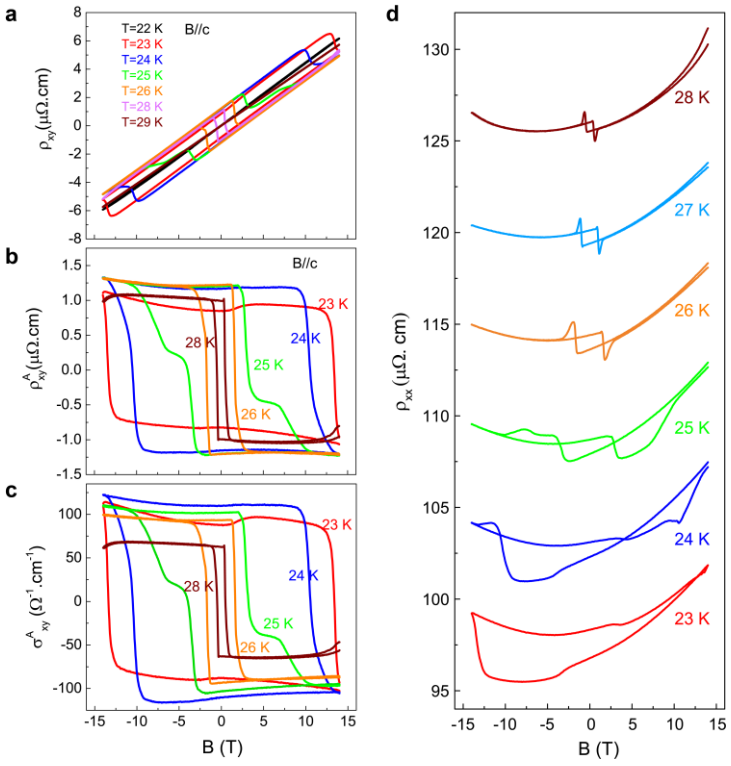

Fig. S14. **a,** Field evolution of the Hall resistivity measured at different temperatures. **b,** Field evolution of the anomalous Hall resistivity obtained by subtracting the ordinary Hall resistivity. **c,** Field evolution of the anomalous Hall conductivity. **d,** Field evolution of the longitudinal resistivity measured at different temperatures.

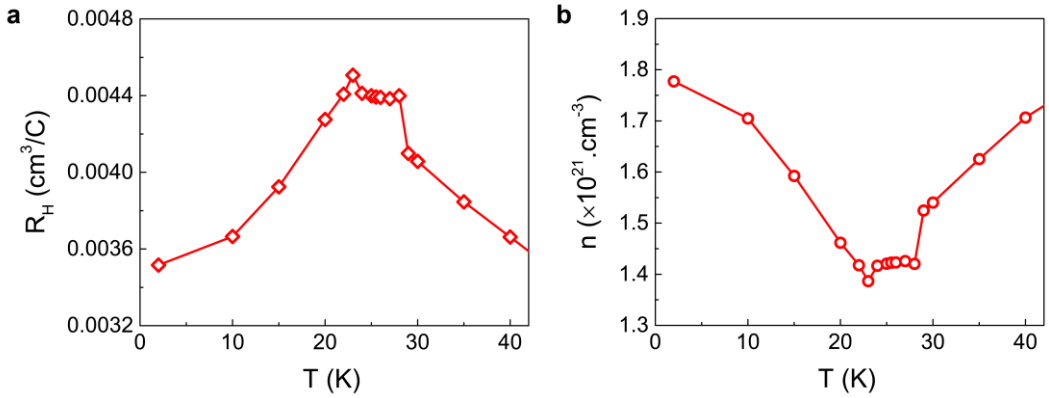

Fig. S15. Temperature dependence of **a,** the ordinary Hall coefficient and **b,** carrier concentration.

S8. Anomalous hall conductivity of $CoNb_3S_6$

S8.1. Anomalous hall conductivity tensors of collinear AFM $CoNb_3S_6$

According to symmetry analysis, the magnetic space group of bulk $CoNb_3S_6$ without/with canting are $P_B2_12_12$ (No. 18.22) and $P2_12_1'2'$ (No. 18.19), respectively. And the magnetic space group of slab $CoNb_3S_6$ without/with canting are P_S1 (No. 1.3) and $P1$ (No. 1.1), respectively. The group elements of these magnetic space groups are listed in Table S3. Bulk and slab $CoNb_3S_6$ without canting are preserved the $T\tau_{\frac{11}{22}0}$. In addition, the main differences between the slab and bulk $CoNb_3S_6$ are all rotation symmetry is broken for slab.

Table S3. Group elements of the magnetic space group describing bulk and slab $CoNb_3S_6$ without/with canting.

	Bulk		Slab	
	w/o canting	w/ canting	w/o canting	w/ canting
Magnetic space group	$P_B2_12_12$	$P2_12_1'2'$	P_S1	$P1$
w/ SOC	E $TC_{2z}\tau_{00\frac{1}{2}}$ $TC_{2y}\tau_{00\frac{1}{2}}$ C_{2x} $T\tau_{\frac{11}{22}0}$ $C_{2z}\tau_{\frac{111}{222}}$ $C_{2y}\tau_{\frac{111}{222}}$ $TC_{2x}\tau_{\frac{11}{22}0}$	E $TC_{2y}\tau_{00\frac{1}{2}}$ $C_{2z}\tau_{\frac{111}{222}}$ $TC_{2x}\tau_{\frac{11}{22}0}$	E $T\tau_{\frac{11}{22}0}$	E

For bulk $CoNb_3S_6$ without canting, the magnetic space group is $P_B2_12_12$ (No. 18.22). Its form of anomalous hall conductivity tensor is $\sigma_{ij}=\begin{pmatrix}\sigma_{xx}&0&0\\0&\sigma_{yy}&0\\0&0&\sigma_{zz}\end{pmatrix}$. Thus the $\sigma_{xy}=0$ for bulk $CoNb_3S_6$ w/o canting. However, when a small canting along the z direction, the magnetic space group becomes $P2_12_1'2'$ (No. 18.19) and the corresponding form of anomalous hall conductivity tensor $\sigma_{ij}=\begin{pmatrix}\sigma_{xx}&\sigma_{xy}&0\\-\sigma_{xy}&\sigma_{yy}&0\\0&0&\sigma_{zz}\end{pmatrix}$, thus $\sigma_{xy}\neq 0$.

For slab $CoNb_3S_6$ w/o canting, the magnetic space group is P_S1 (No. 1.3). Its form of anomalous hall conductivity tensor is $\sigma_{ij}=\begin{pmatrix}\sigma_{xx}&\sigma_{xy}&\sigma_{xz}\\\sigma_{xy}&\sigma_{yy}&\sigma_{yz}\\\sigma_{xz}&\sigma_{yz}&\sigma_{zz}\end{pmatrix}$. The $\sigma_{xy}=\sigma_{yx}$ according to the form of anomalous hall

conductivity tensor. At the same time, σ_{xy} is an antisymmetric tensor, which lead to $\sigma_{xy} = -\sigma_{yx}$. Thus, $\sigma_{xy} = 0$ for slab $CoNb_3S_6$ w/o canting. However, when a small canting along the z direction, the magnetic space group becomes $P1$ (No. 1.1) and the corresponding form of anomalous hall conductivity tensor $\sigma_{ij} = \begin{pmatrix} \sigma_{xx} & \sigma_{xy} & \sigma_{xz} \\ \sigma_{yx} & \sigma_{yy} & \sigma_{yz} \\ \sigma_{zx} & \sigma_{zy} & \sigma_{zz} \end{pmatrix}$, thus $\sigma_{xy} \neq 0$ for slab $CoNb_3S_6$ with canting.

S8.2. Anomalous hall conductivity tensors of triple-q AFM $CoNb_3S_6$

The magnetic space group and spin space group of triple-**q** order [7] (or noncoplanar) are $P32'$ and $P^{3^2_{001}}6_3^{m_{100}}2^{m_{010}}2^{222}1$, respectively (see Table S4). Its form of anomalous hall conductivity tensor is $\sigma_{ij} = \begin{pmatrix} \sigma_{xx} & \sigma_{xy} & 0 \\ -\sigma_{xy} & \sigma_{yy} & 0 \\ 0 & 0 & \sigma_{zz} \end{pmatrix}$, Thus the $\sigma_{xy} \neq 0$ for triple-**q** AFM $CoNb_3S_6$ without net moment. The condition for defining chiral Dirac point is the existence of the doubly degenerate bands in the whole Brillouin zone, which is achieved through a kind of iso-spin symmetry with SU(2) form in the single-**q** structure of $CoNb_3S_6$. In the case of noncoplanar triple-**q** order of $CoNb_3S_6$, the little group at general points for spin space group, denoted as $^{222}1$, cannot guarantee the double degeneracy in the whole Brillouin zone and thus excludes the possibility of chiral Dirac fermions.

Additionally, our DFT calculations also confirm that the triple-**q** $CoNb_3S_6$ without net magnetization, exhibits an anomalous Hall conductivity of approximately 50 $\Omega^{-1}cm^{-1}$ at the Fermi level (Fig. S16b,c).

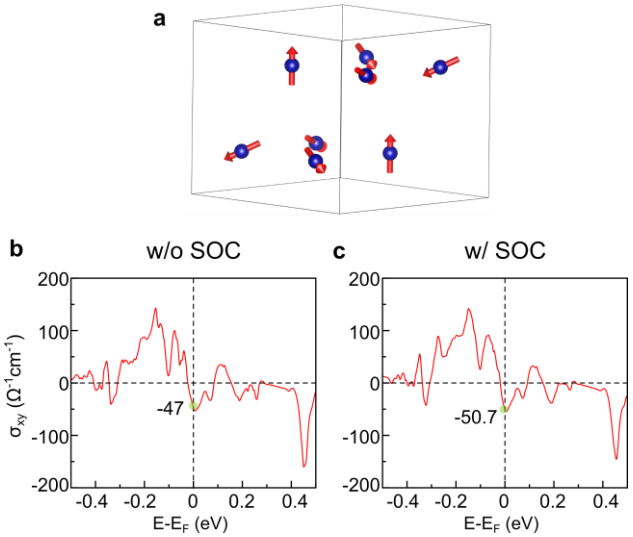

Fig. S16. Anomalous Hall conductivity of noncoplanar $CoNb_3S_6$. **a,** The magnetic structure of triple-**q** AFM $CoNb_3S_6$. **b** and **c** denote the anomalous Hall conductivity with and without SOC, respectively. The anomalous Hall conductivity at the Fermi level is indicated by a cyan circle.

Table S4. Group elements of the magnetic space group and spin group describing triple-**q** $CoNb_3S_6$.

	Generators of group
Magnetic space group ($P32'$)	$\{1\|0\}$, $\{3^1_{001}\|0\}$, $T\{2_{100}\|0\}$
Spin space group ($P^{3^2_{001}}6_3^{m_{100}}2^{m_{010}}2^{222}1$)	$\{1\|\|1\|0\}$, $\{3^1_{001}\|\|3^1_{001}\|0\}$, $\{m_{110}\|\|2_{110}\|0\}$, $\{2_{24\bar{3}}\|\|1\|1/2,0,0\}$, $\{2_{423}\|\|1\|0,1/2,0\}$

S9. Sample dependence of single crystal $Co_xNb_3S_6$

S9.1. Single crystal X-ray diffraction refinements

Single crystals of $CoNb_3S_6$ were grown using chemical vapor transport method. Through a large number of magnetotransport measurements, we found that there are at least four different $Co_xNb_3S_6$ single crystals in the same batch with $0.92 \leq x \leq 1$, which exhibit a substantial anomalous Hall effect tunable by cobalt composition. The crystal structure of $Co_xNb_3S_6$ was characterized using a Bruker D8 Quest diffractometer with Mo-Kα radiation ($\lambda\lambda$ = 0.71069 Å). The data integration and reduction were performed with the commercial Bruker APEX2 software suite. The refined lattice parameters and the atomic occupations for different samples are presented in Tables S5-S12.

Table S5. Single crystal X-ray diffraction refinement for sample1.

Formula	**$Co_{0.92}Nb_3S_6$**
Formula mass (g/mol)	525.11
Crystal system	Hexagonal
Space group	$P6_322$
a (Å)	5.7591(11)
b (Å)	5.7591(11)
c (Å)	11.8520(3)
α	90˚
β	90˚
γ	120˚
V (Å^3)	340.43(9)
T (K)	100
ρ(cal)(g/cm^3)	5.125
λ ($\AA$)	0.71073
F (000)	483.614
Crystal size (mm^3)	0.1 × 0.1 × 0.02
μ (mm^{-1})	9.001
Final R indices	R_1=6.45, ωR_2=8.95
R indices (all data)	R_1=6.69, ωR_2=9.03
Goodness of fit	5.14

Table S6. Wyckoff positions, coordinates, occupancies, and equivalent isotropic displacement parameters for sample1.

Atom	**Wyckoff site**	x	y	z	**Occupancy**	U_{eq}
Co_1	2c	0.333333	0.666667	0.25	0.152804	0.003413
Nb_1	2a	0	0	0	0.166667	0.002596
Nb_2	4f	0.666667	0.333333	0.001660	0.333333	0.002682
S_1	12i	0.332433	0.001140	0.131853	1	0.003157

Table S7. Single crystal X-ray diffraction refinement for sample2.

Formula	**$Co_{0.99}Nb_3S_6$**
Formula mass (g/mol)	529.51
Crystal system	Hexagonal
Space group	$P6_322$
a (Å)	5.7567(6)
b (Å)	5.7567(6)
c (Å)	11.8476(15)
α	90°
β	90°
γ	120°
V (Å^3)	340.02(6)
T (K)	100
ρ(cal)(g/cm^3)	5.174
λ (Å)	0.71073
F (000)	491.539
Crystal size (mm^3)	0.12 × 0.13 × 0.03
μ (mm^{-1})	9.001
Final R indices	R_1=4.21, ωR_2=5.33
R indices (all data)	R_1=4.63, ωR_2=5.40
Goodness of fit	2.70

Table S8. Wyckoff positions, coordinates, occupancies, and equivalent isotropic displacement parameters for sample2.

Atom	**Wyckoff site**	*x*	*y*	*z*	**Occupancy**	U_{eq}
Co_1	2*c*	0.333333	0.666667	0.25	0.165243	0.003942
Nb_1	2*a*	0	0	0	0.166667	0.002660
Nb_2	4*f*	0.666667	0.333333	0.001670	0.333333	0.002636
S_1	12*i*	0.332380	0.001080	0.367970	1	0.003290

Table S9. Single crystal X-ray diffraction refinement for sample3.

Formula	**$Co_{0.98}Nb_3S_6$**
Formula mass (g/mol)	528.76
Crystal system	Hexagonal
Space group	$P6_322$
a (Å)	5.7490(2)
b (Å)	5.7490(2)
c (Å)	11.8960(3)
α	90°
β	90°
γ	120°
V (Å^3)	340.20(5)
T (K)	100
ρ(cal)(g/cm^3)	5.164
λ (Å)	0.71073
F (000)	490.852
Crystal size (mm^3)	0.12 × 0.12 × 0.03
μ (mm^{-1})	9.001
Final R indices	R_1=1.76, ωR_2=4.61
R indices (all data)	R_1=1.91, ωR_2=4.65
Goodness of fit	3.52

Table S10. Wyckoff positions, coordinates, occupancies, and equivalent isotropic displacement parameters for sample3.

Atom	**Wyckoff site**	*x*	*y*	*z*	**Occupancy**	U_{eq}
Co_1	2*c*	0.333333	0.666667	0.25	0.163125	0.003250
Nb_1	2*a*	0	0	0	0.166667	0.002521
Nb_2	4*f*	0.666667	0.333333	0.001630	0.333333	0.002523
S_1	12*i*	0.332440	0.001140	0.36807	1	0.003313

Table S11. Single crystal X-ray diffraction refinement for sample4.

Formula	**$CoNb_3S_6$**
Formula mass (g/mol)	530.1
Crystal system	Hexagonal
Space group	$P6_322$
a (Å)	5.7637(4)
b (Å)	5.7637(4)
c (Å)	11.8876(7)
α	90°
β	90°
γ	120°
V (Å^3)	342.00(1)
T (K)	100
ρ(cal)(g/cm^3)	5.150
λ ($\AA$)	0.71069
F (000)	489.758
Crystal size (mm^3)	0.15 × 0.12 × 0.05
μ (mm^{-1})	9.001
Final R indices	R_1=2.31, ωR_2=4.71
R indices (all data)	R_1=2.46, ωR_2=4.76
Goodness of fit	3.59

Table S12. Wyckoff positions, coordinates, occupancies, and equivalent isotropic displacement parameters for sample4.

Atom	**Wyckoff site**	x	y	z	**Occupancy**	U_{eq}
Co_1	2c	0.333333	0.666667	0.25	0.166859	0.003231
Nb_1	2a	0	0	0	0.166667	0.001903
Nb_2	4f	0.666667	0.333333	0.001647	0.333333	0.001906
S_1	12i	0.332438	0.001157	0.131880	1	0.002675

S9.2. Magnetotransport measurements for different samples

The magnetotransport data of the above four samples are presented in Fig. S17. $Co_xNb_3S_6$ undergo an antiferromagnetic phase transition at $T_N = 26.3$ K for $x = 0.92$ (Fig. S17a), and four antiferromagnetic phase transitions at $T_{N_1} = 28.2$ K, $T_{N_2} = 26.7$ K, $T_{N_3} = 24.9$ K, $T_{N_4} = 22.5$ K for $x = 0.99$ (Fig. S17b). For both these two samples, there are no ferromagnetic components or AHE observed (as shown in Figs. S17e,f and Figs. S17i,j). Furthermore, our single crystal neutron diffraction experiment shows that $Co_{0.92}Nb_3S_6$ (the sample without AHE) also shares same collinear magnetic structure (Γ_4) with $CoNb_3S_6$, which illustrates that the collinear magnetic structure alone cannot explain the large AHE observed in $CoNb_3S_6$. (more details are presented in Fig. S6).

As a comparison, weak ferromagnetic components and AHE appeared simultaneously in $Co_xNb_3S_6$ with $x =$

0.98, 1.0 (as shown in Figs. S17g,h and Figs. S17k,l), which indicates that the weak ferromagnetic components play an important role to the AHE observed in $Co_xNb_3S_6$. More importantly, such observation suggests that crystal Hall effect [8] mechanism is insufficient in elucidating the anomalous Hall effect observed in $CoNb_3S_6$. This is because crystal Hall effect would still exist given the ideal antiferromagnetic configuration (no magnetic canting). In the main text, we chose $CoNb_3S_6$ as the research object.

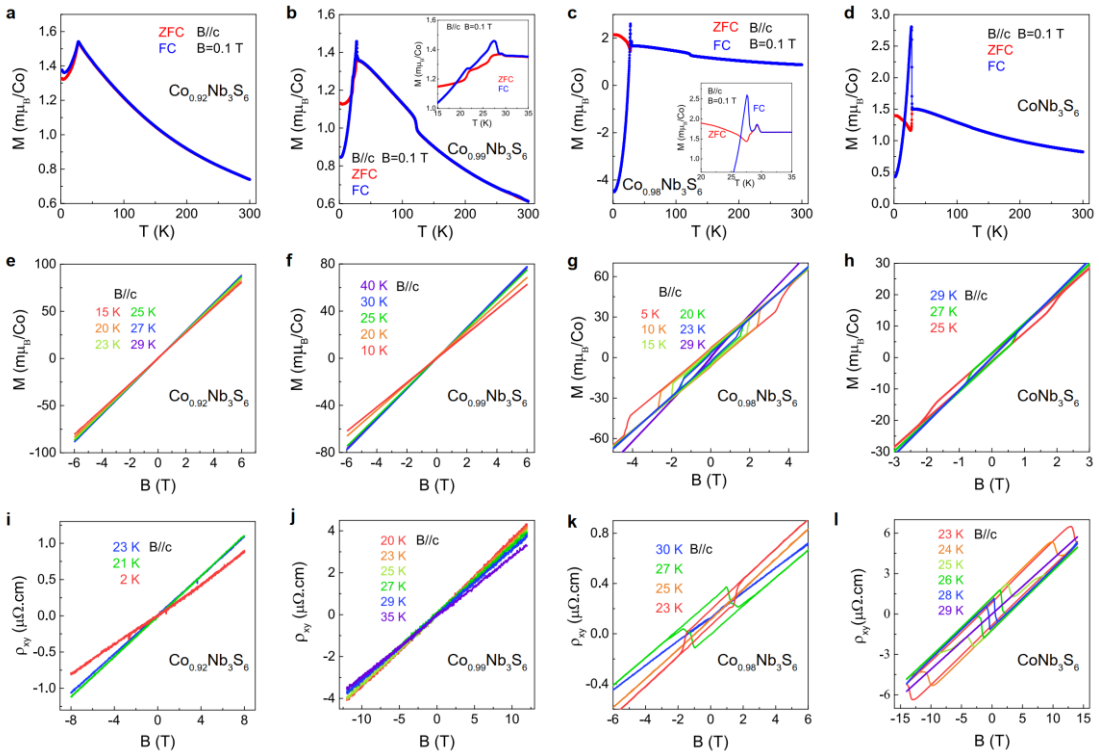

Fig. S17. Magnetization and anomalous Hall effect measurements for different samples $Co_xNb_3S_6$ with x = 0.92, 0.99, 0.98, 1.0, respectively. **a-d** Temperature dependence of the magnetization measured at $B = 0.1$ T with $B//c$ for different samples. **e-h** Field dependence of the magnetization measured at different temperatures with $B//c$ for different samples. **i-l** Hall effects measured at different samples with $B//c$.

S10. The Fermi surface of triple-q $CoNb_3S_6$

Recently, a triple-**q** (or noncoplanar) antiferromagnetic (AFM) has been proposed in $CoNb_3S_6$ [7]. Our Fermi surface results suggests that noncoplanar AFM may not the realistic magnetic structure of $CoNb_3S_6$. We compared the Fermi surfaces of noncoplanar magnetic structures with those observed through ARPES. Firstly, the noncoplanar AFM structure constitutes a 2 × 2 supercell compared with the nonmagnetic primitive cell (ARPES). The size of the Brillouin zone (BZ) corresponding to the noncoplanar AFM with different termination (The red hexagon shown in Fig. S18a,b) does not align with the size of ARPES Brillouin zone (The black hexagon shown in Fig. S18c). Additionally, the Fermi surface of noncoplanar AFM apparently fails to reproduce the ARPES Fermi surface (Fig. S18a-c) since no band-folding signature appears on the boundary of noncoplanar AFM Brillouin zone in ARPES data (Fig. S18c). Conversely, the Fermi surface of collinear AFM of $CoNb_3S_6$ demonstrates better agreement with the experimental results (Fig. S18c,d).

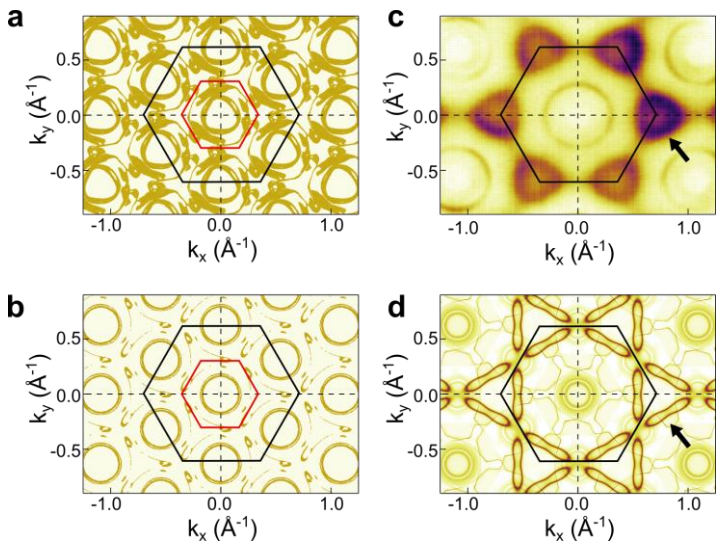

Fig. S18. Fermi surface of $CoNb_3S_6$. **a,b** DFT calculated Fermi surfaces with only surface state spectral weight for noncoplanar $CoNb_3S_6$ with different termination. **c** denotes the ARPES Fermi surface mapping and **d** DFT calculated Fermi surfaces with only surface state spectral weight based on collinear AFM order. The black arrow in **c** and **d** indicates the β pocket. The black and red hexagon denotes the nonmagnetic surface BZ and noncoplanar AFM surface BZ, respectively.

Supplementary references

[1] S. Coleman and J. Mandula, Phys. Rev. **159**, 1251 (1967).

[2] W. Heisenberg, Zeitschrift für Physik **77**, 1 (1932).

[3] S. Weinberg, The quantum theory of fields (Cambridge university press, 1995), Vol. 2.

[4] S. S. P. Parkin, E. A. Marseglia, and P. J. Brown, J. Phys. C: Solid State Phys **16**, 2765 (1983).

[5] K. Lu *et al.*, arXiv:2212.14762 (2022).

[6] P. Liu, A. Zhang, J. Han, and Q. Liu, The Innovation **3**, 100343 (2022).

[7] H. Takagi *et al.*, Nat. Phy. **19**, 961 (2023).

[8] L. Šmejkal, R. González-Hernández, T. Jungwirth, and J. Sinova, Sci. Adv. **6**, eaaz8809 (2020).